The Astrophysical Journal, 781:69 (18pp), 2014 February 1 doi:10.1088/0004-637X/781/2/69

TYPE IIb SUPERNOVA SN 2011dh: SPECTRA AND PHOTOMETRY FROM THE ULTRAVIOLET TO THE NEAR-INFRARED

G. H. Marion[1,2], Jozsef Vinko[2,3], Robert P. Kirshner[1], Ryan J. Foley[1,14], Perry Berlind[1], Allyson Bieryla[1], Joshua S. Bloom[4], Michael L. Calkins[1], Peter Challis[1], Roger A. Chevalier[5], Ryan Chornock[1], Chris Culliton[6], Jason L. Curtis[6], Gilbert A. Esquerdo[1], Mark E. Everett[7], Emilio E. Falco[1], Kevin France[8], Claes Fransson[9], Andrew S. Friedman[1], Peter Garnavich[10], Bruno Leibundgut[11], Samuel Meyer[1], Nathan Smith[12], Alicia M. Soderberg[1], Jesper Sollerman[10], Dan L. Starr[5], Tamas Szklenar[1], Katalin Takats[3,13], and J. Craig Wheeler[2]

[1] Harvard-Smithsonian Center for Astrophysics, 60 Garden St., Cambridge, MA 02138, USA; gmarion@cfa.harvard.edu
[2] University of Texas at Austin, 1 University Station C1400, Austin, TX 78712-0259, USA
[3] Department of Optics and Quantum Electronics, University of Szeged, Domter 9, 6720 Szeged, Hungary
[4] Department of Astronomy, University of California, Berkeley, CA 94720-3411, USA
[5] Astronomy Department, University of Virginia, Charlottesville, VA 22904, USA
[6] Department of Astronomy and Astrophysics, Pennsylvania State University, 525 Davey Laboratory, University Park, PA 16802, USA
[7] National Optical Astronomy Observatory, Tucson, AZ 85719, USA
[8] Center for Astrophysics and Space Astronomy, University of Colorado, 389 UCB, Boulder, CO 80309, USA
[9] Department of Astronomy, The Oskar Klein Centre, Stockholm University, S-106 91 Stockholm, Sweden
[10] Department of Physics, University of Notre Dame, 225 Nieuwland Science Hall, Notre Dame, IN 46556, USA
[11] European Southern Observatory, D-85748 Garching bei München, Germany
[12] University of Arizona, Steward Observatory, Tucson, AZ 85721, USA
[13] Departamento de Ciencias Fisicas, Universidad Andres Bello, Avda. Republica 252, Santiago, Chile
Received 2013 March 21; accepted 2013 December 9; published 2014 January 9

ABSTRACT

We report spectroscopic and photometric observations of the Type IIb SN 2011dh obtained between 4 and 34 days after the estimated date of explosion (May 31.5 UT). The data cover a wide wavelength range from 2000 Å in the ultraviolet (UV) to 2.4 μm in the near-infrared (NIR). Optical spectra provide line profiles and velocity measurements of H I, He I, Ca II, and Fe II that trace the composition and kinematics of the supernova (SN). NIR spectra show that helium is present in the atmosphere as early as 11 days after the explosion. A UV spectrum obtained with the Space Telescope Imaging Spectrograph reveals that the UV flux for SN 2011dh is low compared to other SN IIb. Modeling the spectrum with SYNOW suggests that the UV deficit is due to line blanketing from Ti II and Co II. The H I and He I velocities in SN 2011dh are separated by about 4000 km s^{-1} at all phases. A velocity gap is consistent with models for a preexplosion structure in which a hydrogen-rich shell surrounds the progenitor. We estimate that the H shell of SN 2011dh is ≈8 times less massive than the shell of SN 1993J and ≈3 times more massive than the shell of SN 2008ax. Light curves (LCs) for 12 passbands are presented: *UVW2*, *UVM2*, *UVW1*, U, u', B, V, r', i', J, H, and K_s. In the B band, SN 2011dh reached peak brightness of 13.17 mag at 20.0 ± 0.5 after the explosion. The maximum bolometric luminosity of $1.8 \pm 0.2 \times 10^{42}$ erg s^{-1} occurred ≈22 days after the explosion. NIR emission provides more than 30% of the total bolometric flux at the beginning of our observations, and the NIR contribution increases to nearly 50% of the total by day 34. The UV produces 16% of the total flux on day 4, 5% on day 9, and 1% on day 34. We compare the bolometric LCs of SN 2011dh, SN 2008ax, and SN 1993J. The LC are very different for the first 12 days after the explosions, but all three SN IIb display similar peak luminosities, times of peak, decline rates, and colors after maximum. This suggests that the progenitors of these SN IIb may have had similar compositions and masses, but they exploded inside hydrogen shells that have a wide range of masses. SN 2011dh was well observed, and a likely progenitor star has been identified in preexplosion images. The detailed observations presented here will help evaluate theoretical models for this SN and lead to a better understanding of SN IIb.

Key words: infrared: general – supernovae: general – supernovae: individual (2011dh) – ultraviolet: general

Online-only material: color figures

1. INTRODUCTION

SN 2011dh (= PTF11eon) was discovered in the nearby "Whirlpool" galaxy M51 ($D \approx 8.05$ Mpc) less than a day after the explosion. The early detection and close proximity of SN 2011dh provide optimal conditions for detailed observations of the supernova (SN).

Core-collapse SNe are classified according to their observational characteristics. Type II SN are hydrogen rich, and their spectra display prominent Balmer series features. SN Ib do not have hydrogen features in their spectra, but helium is clearly detected. The spectra of SN Ic lack features of both hydrogen and helium. This sequence is usually interpreted as evidence for progressive stripping of hydrogen and helium from the outer atmosphere of the progenitor star. The stripping may be due to stellar winds or mass transfer to a companion star. SN Ib and SN Ic are often described as "stripped-envelope core-collapse" (SECC) events.

Type IIb SNe may form a separate class, or they may be part of a continuum of related SN. The spectra of SN IIb display

[14] Clay Fellow, Harvard-Smithsonian Center for Astrophysics

strong hydrogen features at early phases with no evidence for helium. He features appear after about two weeks, and they become stronger with time as the H features weaken rapidly. The weakness of H features in SN IIb suggests that they are related to the SECC group. SN IIb have been proposed as an intermediate step between SN II and SN Ib (Filippenko et al. 1993; Nomoto et al. 1993; Woosley et al. 1994). For a review of the relationship between SN classifications and progenitor structure, see Nomoto et al. (1995).

There are two proposed progenitor channels for SN IIb: an isolated star ($\gtrsim$25 $M_{\odot}$) that loses most of its hydrogen envelope through stellar winds (e.g., Chiosi & Maeder 1986) and a close binary system where mass transfer strips most of the hydrogen from the outer layers of the progenitor star (e.g., Podsiadlowski et al. 1993). The progenitor in the mass transfer model may be relatively low mass and compact, similar to a Wolf–Rayet star (Dessart et al. 2011).

The immediate postexplosion luminosity of SN IIb is produced by a hot atmosphere that has been heated by the shock from the explosion. The SN luminosity fades as the shocked atmosphere expands and cools. SN IIb from compact progenitors are expected to display relatively weak early emission from the shock-heated atmosphere with the thermal powered luminosity declining rapidly (a few days) after the explosion (Chevalier & Soderberg 2010). This behavior was observed in SN 2008ax (Pastorello et al. 2008; Roming et al. 2009; Chornock et al. 2011; Taubenberger et al. 2011). On the other hand, SN IIb with more mass and extended radii in their hydrogen envelopes are expected to have longer cooling times, such as ∼20 days observed for SN IIb 1993J (Schmidt et al. 1993; Wheeler et al. 1993; Lewis et al. 1994; Richmond et al. 1994, 1996). A decline in the observed brightness of SN 2011dh is reported from day 1 to day 3, which is consistent with this cooling (Maund et al. 2011; Arcavi et al. 2011; Bersten et al. 2012; Tsvetkov et al. 2012).

A second luminosity source is provided by radioactivity in the SN core. The contribution from the core increases with time, and within a few days it is equal to the declining thermal luminosity. From that minimum, the SN brightness increases until it reaches the second, or radiation, peak. An initial thermal maximum, a decline to a minimum, and a subsequent rise to a second maximum have been observed in the light curves (LCs) of several SECC SN: SN IIb 1993J (Schmidt et al. 1993; Wheeler et al. 1993; Lewis et al. 1994; Richmond et al. 1994, 1996), SN IIb 2008ax (Pastorello et al. 2008; Roming et al. 2009; Chornock et al. 2011; Taubenberger et al. 2011), SN IIb 2011fu (Kumar et al. 2013), SN Ib 2008D (Modjaz et al. 2009), and the peculiar SN II 1987A (Arnett et al. 1989).

The first spectrum of SN 2011dh was obtained by Silverman et al. (2011) less than 3 days after discovery. The presence of strong Balmer lines and the absence of helium led them to classify SN 2011dh as an SN II. Other reports noted similarities between the early spectra of SN 2011dh and Type IIb SN 1993J without identifying He features (Maund et al. 2011; Arcavi et al. 2011). Marion et al. (2011) confirmed the Type IIb classification by identifying He I lines in near-infrared (NIR) spectra obtained 16 days after the explosion (≈3 days prior to the *B*-band peak). The final version of Maund et al. (2011) discusses He I lines in optical spectra obtained 20, 30, and 40 days after the explosion.

Some authors find evidence for a compact progenitor of SN 2011dh. Van Dyk et al. (2011), Prieto & Hornoch (2011), Arcavi et al. (2011), Soderberg et al. (2012), Krauss et al. (2012), and Bietenholz et al. (2012) use optical, radio, and X-ray observations and theory to suggest that the progenitor of SN 2011dh had a radius of the order of 1 $R_{\odot}$. Horesh et al. (2013) derive an intermediate preexplosion radius and suggest that a continuum of sizes for SN IIb progenitors exists rather than a bimodal distribution consisting only of compact or extended stars.

Other authors conclude that the progenitor of SN 2011dh had an extended radius such as that found in a supergiant-type star. The location of SN 2011dh was imaged by the *Hubble Space Telescope* (*HST*) in multiple filters prior to the explosion, and a yellow supergiant star has been identified near the position of the explosion. An active debate in the literature discusses whether or not this star is a plausible progenitor. Observational evidence in support of the yellow supergiant as the progenitor for SN 2011dh is presented by Maund et al. (2011) and Murphy et al. (2011). Theoretical support for the interpretation that the progenitor had an extended radius ($\geqslant$200 $R_{\odot}$) is provided by Bersten et al. (2012), Benvenuto et al. (2013), and Ergon et al. (2013).

Almost 700 days after the explosion, Van Dyk et al. (2013) observed the location of SN 2011dh with *HST* Wide Field Camera 3 (WFC3) and determined that the yellow supergiant star in that area has disappeared. Their result suggests that the yellow supergiant was correctly identified as the progenitor, and theoretical explanations can now focus on much more specific physical models.

Here, we report high-cadence observations of SN 2011dh obtained between 4 and 34 days after the estimated date of explosion (May 31.5 UT). Both photometric and spectroscopic data cover a wide wavelength range from 2000 Å in the ultraviolet (UV) to 2.4 μm in the NIR. The detailed observations of SN 2011dh presented here will help constrain theoretical models of SN IIb and contribute to an improved understanding of SN IIb and all SECC SNe.

The chemical structure of SN 2011dh is explored by measuring line profiles and velocities for absorption features in the spectra. Velocity measurements reveal the relative locations of line-forming regions in radial space, and the changing strengths of the lines with time provide clues about the relative abundances. Observations with the Space Telescope Imaging Spectrograph (STIS) on *HST* and the *Swift* U grism provide rare UV spectroscopy of a SN IIb and extend the range of our spectroscopic analysis.

LCs are presented for 12 passbands: *UVW2*, *UVM2*, *UVW1*, U, u', B, V, r', i', J, H, and K. We construct a bolometric LC for SN 2011dh and compare the result to a bolometric LC for SN 2011dh reported by Ergon et al. (2013). We also compare the bolometric LCs of SN IIb 1993J (Richmond et al. 1996) and SN IIb 2008ax (Pastorello et al. 2008). The LCs for these SN IIb display many similarities after the initial period of influence from the thermal luminosity.

The data acquisition and reduction details are presented in Section 2. Spectral features are identified and discussed in Section 3. Velocity measurements are described in Section 4, including a discussion of the gap between H I and He I velocities. Synthetic spectra from SYNOW are used to confirm line identifications and to discuss physical properties in Section 5. Multiband LCs and color evolution are presented and discussed in Section 6. The bolometric LC is described in Section 7 and compared to other bolometric LC for SN IIb. Temperature estimates are discussed in Section 8. A summary and conclusions are presented in Section 9.

2. OBSERVATIONS

The Whirlpool galaxy (M51) is a lovely galaxy that is frequently imaged by professionals and amateurs. SN 2011dh was not detected in an image obtained by the Palomar Transient Factory (PTF) on May 31.275 to a limiting magnitude of $g = 21.44$. The first detection of SN 2011dh was by amateur A. Riou on May 31.893 (UT), and there were several independent discoveries soon thereafter (Reiland et al. 2011). The PTF also made an independent discovery on June 1.191, and many early sources reference the SN with the PTF name: PTF11eon. For this paper, we adopt an explosion date of May 31.5 UT (MJD 55712.5), and we express the times of all observations in days relative to the explosion. Uncertainties of a few hours for the time of t_0 do not affect the presentation of our results or our conclusions.

Distance measurements for M51 have a significant scatter. Tonry et al. (2001) use surface brightness fluctuations (SBFs) to determine $D = 7.7 \pm 0.9$ Mpc. However, M51 is a large spiral galaxy, and there may be significant dust present that would compromise the effectiveness of the SBF method. The Tonry et al. (2001) result matches the value of $D = 7.7 \pm 1.3$ Mpc found in the Nearby Galaxies Catalog that was determined using the Tully–Fisher method (Tully 1988). A higher value for D is found by Vinkó et al. (2012), who use the expanding photosphere method to measure the distance to M51 as $D = 8.4 \pm 0.7$ Mpc. Feldmeier et al. (1997) also measure $D = 8.4 \pm 0.6$ Mpc using a planetary nebula luminosity function.

For this paper, we use the mean value of these four measurements for calculations that include distance ($D = 8.05$ Mpc). We note that the maximum difference of ± 0.35 Mpc between our adopted value for D and any of the referenced measurements introduces only ± 0.1 mag uncertainty in the luminosity measurements. Such a small difference has no significant effect on our results. We use a heliocentric velocity of 600 km s^{-1} (NASA/IPAC Extragalactic Database; Rush et al. 1996) to correct wavelength measurements to the rest frame.

Extinction from the host is low. Vinkó et al. (2012) and Arcavi et al. (2011) do not detect Na D lines at the redshift of M51 in high-resolution spectra. Arcavi et al. (2011) set an upper limit on extinction from the host at $E(B - V) < 0.05$ mag. Ritchey & Wallerstein (2012) identify weak absorption components from Na D and Ca II H&K in high-dispersion spectra, but they conclude that the overall weakness of the Na D detection confirms a low foreground and host galaxy extinction. The *HST*/STIS spectrum in our sample shows interstellar Mg II (λ2795) absorption with an equivalent width of approximately 1 Å, which is consistent with the assumption of low extinction.

Galactic extinction is $E(B - V) = 0.035$ mag (Schlegel et al. 1998), so that the V-band extinction correction is $\approx$0.1 mag. We correct for Milky Way extinction when constructing the bolometric luminosity, but in the figures and tables we present the measured values.

2.1. Spectroscopy

Figure 1 shows 26 spectra of SN 2011dh obtained between 4 and 34 days after the explosion. The sample includes optical spectra (3480–7420 Å) obtained at the F. L. Whipple Observatory (FLWO) 1.5 m Tillinghast telescope using the FAST spectrograph (Fabricant et al. 1998) on days 4–9, 24–28, 30–32, and 34 with respect to the time of explosion. FLWO/FAST data are reduced using a combination of standard IRAF and custom IDL procedures (Matheson et al. 2005).

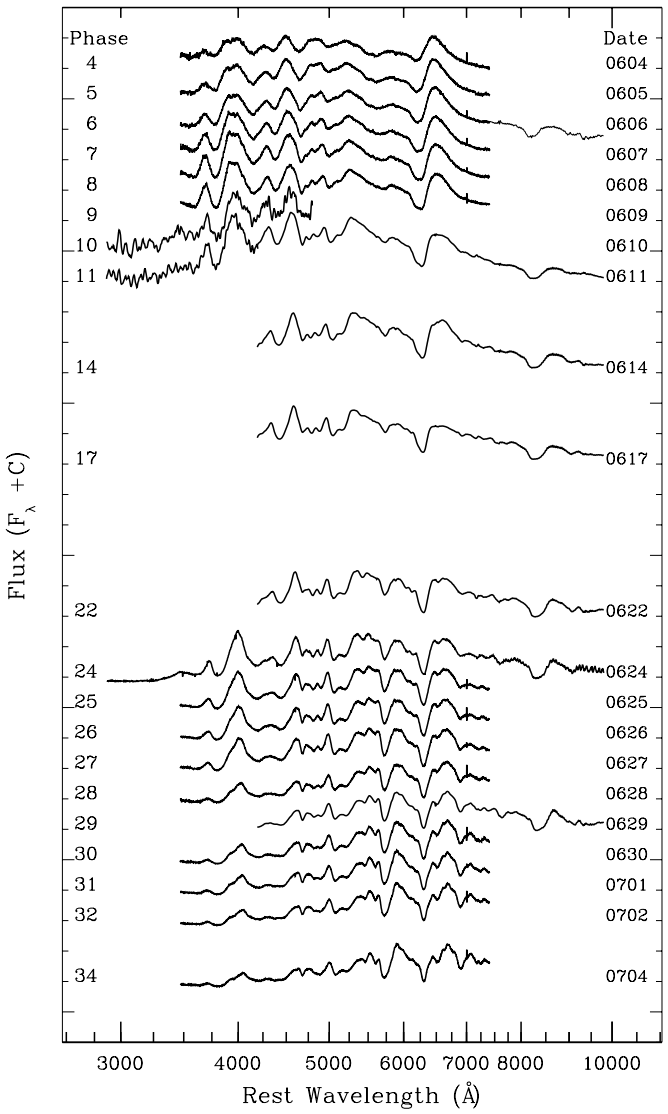

Figure 1. UV and optical spectra from SN 2011dh from 4 to 34 days after the explosion. Data were obtained with *HST*/STIS (day 24, 2800–10000 Å), Tillinghast/FAST (3400–7400 Å), HET/LRS (4200–10000 Å), and *Swift*/UV grism (days 10 and 11, 2800–4600 Å). The phase with respect to the explosion is displayed to the left of each spectrum, and the dates of observation are listed to the right. Spectral features are discussed in Section 3. Observing details are listed in Table 1.

Additional optical spectra (4200–10100 Å) were obtained on days 6, 11, 14, 17, 22, and 29 with the 9.2 m Hobby–Eberly Telescope (HET; Ramsey et al. 1998) at the McDonald Observatory using the Marcario Low-Resolution Spectrograph (LRS; Hill et al. 1998). HET/LRS spectra are reduced with standard IRAF procedures. On some of the nights, two spectra were obtained that cover different wavelength regions. In those cases, the spectra were combined to form a single spectrum for each phase. The observational details are given in Table 1.

Low ($R \approx 200$, $\lambda = 0.65$–$2.5\,\mu$m) and medium ($R \approx 1200$, $\lambda = 0.80$–$2.4\,\mu$m) resolution NIR spectra were obtained on days 8, 12, and 16 with the 3 m telescope at the NASA Infrared Telescope Facility (IRTF) using the SpeX medium-resolution spectrograph (Rayner et al. 2003). Figure 2 displays the NIR spectra with nearly contemporaneous optical spectra. IRTF data are reduced using a package of IDL routines specifically designed for the reduction of SpeX data (Spextool v. 3.4; Cushing et al. 2004).

Table 1
Spectroscopic Observations of SN 2011dh

Date[a] (UT)	Instrument	Range (Å)	R	Exp. (s)
Jun 4.2	FAST	3480–7420	1350	900
Jun 5.2	FAST	3480–7420	1350	1500
Jun 6.1	HET	4200–10100	280	900
Jun 6.2	FAST	3480–7420	1350	1200
Jun 7.2	FAST	3480–7420	1350	1200
Jun 8.2	FAST	3480–7420	1350	900
Jun 8.4	IRTF	8000–24000	1200	1800
Jun 9.2	FAST	3480–7420	1350	900
Jun 9.9	SWIFT	2000–4600	150	900
Jun 11.1	SWIFT	2000–4600	150	1135
Jun 11.2	HET	4200–10100	280	900
Jun 12.4	IRTF	8000–24000	1200	1800
Jun 14.2	HET	4200–10000	280	900
Jun 16.4	IRTF	8000–24000	1200	1800
Jun 17.2	HET	4200–10100	280	900
Jun 22.2	HET	4200–10100	280	900
Jun 24.0	HST	2160–10230	4300	3600
Jun 25.2	FAST	3480–7420	1350	720
Jun 26.2	FAST	3480–7420	1350	720
Jun 27.2	FAST	3480–7420	1350	720
Jun 28.3	FAST	3480–7420	1350	840
Jun 29.2	HET	4200–10100	280	900
Jun 30.3	FAST	3480–7420	1350	900
Jul 1.2	FAST	3480–7420	1350	900
Jul 2.2	FAST	3480–7420	1350	960
Jul 4.2	FAST	3480–7420	1350	900

Notes. The time of explosion is approximately May 31.5 UT, and the time of B max is approximately June 20 UT.
[a] All observations in 2011.

Table 2
Peak Magnitudes and Filter Details

Band	M_{peak} (mag)	D_{peak}[a]	N_{obs}	λ_{mid} (Å)
		PAIRITEL[b]		
K_s	<11.91[c]	>24[c]	18	21590
H	<11.91[c]	>24[c]	18	16620
J	<12.02[c]	>24[c]	17	12350
		KeplerCam		
i'	12.45	23.2	27	7747
r'	12.26	21.7	27	6217
V	12.44	20.6	26	5375
B	13.17	20.0	25	4270
u'	14.42	16.6	14	3525
		Swift		
V	12.63	20.9	37	5468
B	13.39	19.5	39	4392
U	13.90	16.5	40	3465
UVW1	15.53	15.1	27	2600
UVM2	...	...	27	2246
UVW2	...	...	27	1928

Notes. Systematic offsets of $u' = -0.05$ mag, $B = +0.15$ mag, $V = +0.11$ mag, $r' = -0.04$ mag, and $i' = +0.08$ mag are found between the FLWO 1.2 m data and other published data (see Section 2.2). Accounting for these offsets, the FLWO light curves match Arcavi et al. (2011, i') and Tsvetkov et al. (2012, $u'BVr'$) within ±0.05 mag.
[a] Whole days with respect to the time of explosion.
[b] Filter details from Cohen et al. (2003).
[c] Final measurements on day 24 precede the peak by a day or two.

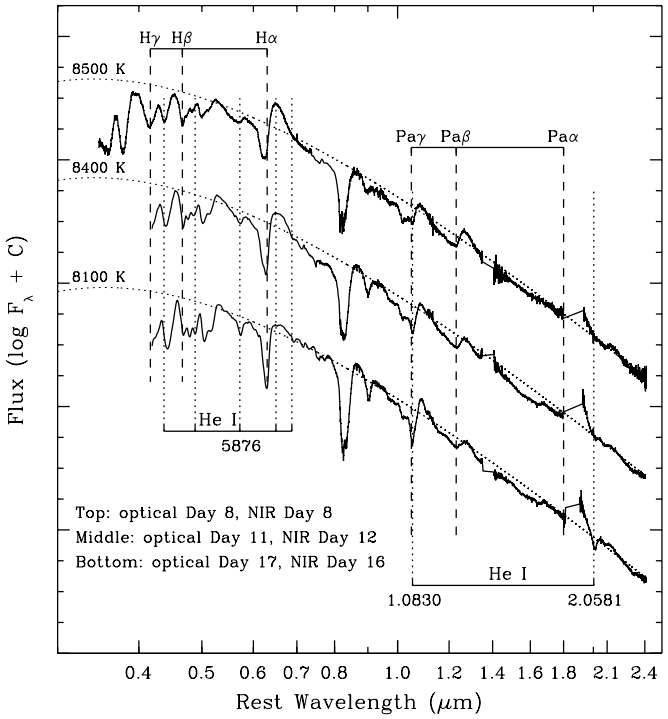

Figure 2. Optical and NIR spectra of SN 2011dh from 0.32 to 2.4μm obtained 8 to 17 days after the explosion. H I is strong at these early phases, and Balmer and Paschen lines (α, β, and γ) are marked at 12,000 km s^{-1}. Several He I lines are marked at 8000 km s^{-1}, with the NIR λλ1.0830, 2.0581 and the optical λ5876 lines labeled. He I is not detected on day 8 (top). The combined evidence of the labeled He I features suggests that He I is present on days 11 and 12 (middle). He I features are obvious on day 16 (bottom). The dotted lines are blackbody temperature curves.

Low-resolution UV spectra were obtained by *Swift* with the UVOT U grism (2000–4600 Å) on days 10 and 11. The data were downloaded from the *Swift* archive.[15] *Swift* data are analyzed within HEAsoft following the standard recipe in the "UVOT User's Guide."[16] The raw frames are converted into "DET" images by applying the `swiftxform` task after flat fielding and bad-pixel masking. The final spectra are extracted and calibrated with the `uvotimgrism` task. Wavelength and flux calibrations are corrected by matching the U-grism spectra with contemporaneous ground-based spectra covering 3000–5000 Å.

A spectrum of SN 2011dh was obtained on day 24 with STIS on the *HST* under observing program GO-12540 (PI: R. P. Kirshner). Three STIS gratings were employed with the CCD detector G230LB (3600 s), G430L (800 s), and G750L (350 s), and the combined spectrum covers 2160–10230 Å. The *HST* data are reduced using the Space Telescope Science Institute STIS pipeline.

2.2. Photometry

Photometry of SN 2011dh was obtained in 12 filters, and the LCs are displayed in Figure 3. Table 2 gives the peak magnitudes and dates of peak for each passband. The values were determined by fitting a parabola to the data. The central wavelengths for each filter are also in Table 2.

SN 2011dh was observed at the FLWO with the 1.2 m telescope and the KeplerCam instrument in the *uBVri* bands

[15] http://heasarc.gsfc.nasa.gov/docs/swift/archive/
[16] http://heasarc.gsfc.nasa.gov/docs/swift/analysis/; UVOT_swguide_v2_2.pdf

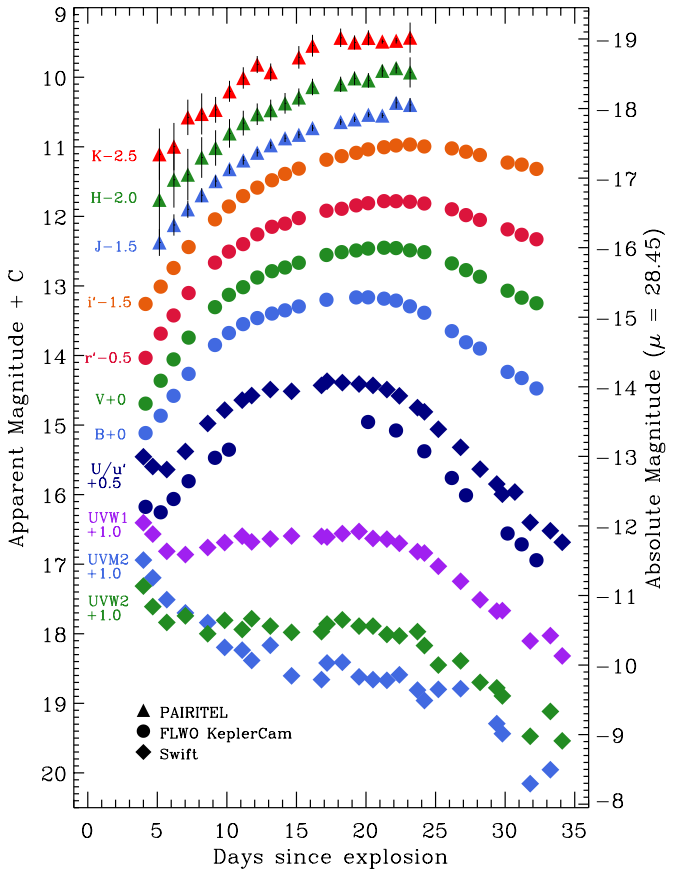

Figure 3. UVOIR photometry of SN 2011dh in 12 filters obtained on days 4–34 by the *Swift* satellite, the FLWO 1.5 m with KeplerCam, and the FLWO 1.3 m with PAIRITEL. Uncertainties are smaller than the symbols used for plotting except where indicated for some of the PAIRITEL data. The *Swift U* band and the KeplerCam u' band are plotted with the same offset, and the light curves are different by about 0.5 mag. We fit the data for each filter with a polynomial and list the peak magnitudes, dates of peak, and the central wavelengths in Table 2. SN 2011dh had not reached maximum in the NIR before the final JHK_s observations on day 24.

(A color version of this figure is available in the online journal.)

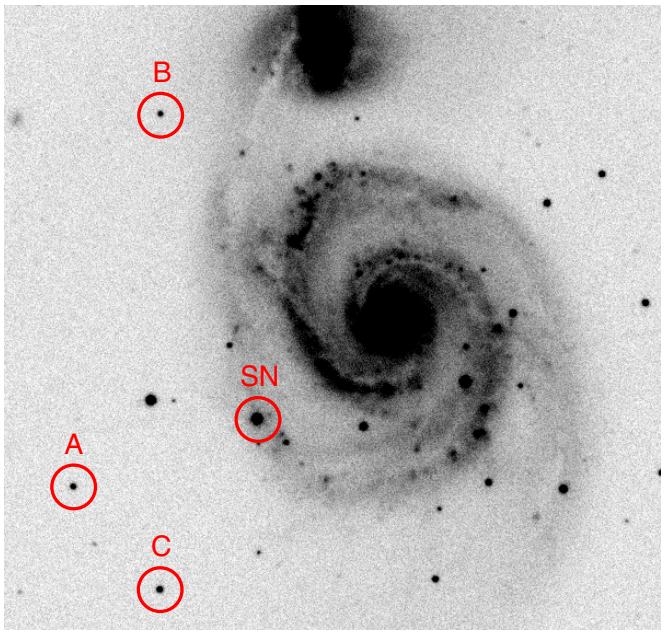

Figure 4. M51, SN 2011dh, and local comparison stars used for differential photometry on nonphotometric nights. (See Table 4 and Section 2.2.)

(A color version of this figure is available in the online journal.)

(Table 3). The KeplerCam data are reduced using IRAF and IDL procedures as described in Hicken et al. (2007). These data have not been *s* corrected, and no host-galaxy subtraction was performed since the SN was well separated from the galaxy center and other stars. The $u'BVr'i'$ instrumental magnitudes were measured with point-spread function (PSF) fitting on template-subtracted images using the methods described in Hicken et al. (2012).

Transformation to the standard photometric system was performed using local comparison stars around the SN in the same field of view. The linear transformation equations were calibrated using Landolt (1992) standards for *UBV* and Smith et al. (2002) standards for r' and i' bands. For u' we transformed the Landolt (1992) *U*-band magnitudes to u' via the equation $u' = U + 0.854$ mag (Chonis & Gaskell 2008). The zero points of the transformations were determined on five photometric nights. The zero points for images obtained on nonphotometric nights were determined by differential photometry using local comparison stars as anchors (see Table 4 and Figure 4). Note that our *BV* data are in Vega magnitudes, while the $u'r'i'$ data are in AB magnitudes.

The r'- and i'-band measurements of the field stars were checked against their magnitudes in the Sloan Digital Sky Survey DR10 database. The values were in agreement to ≈0.02 mag. The same level of agreement was found when comparing the common field stars with the measurements by Arcavi et al. (2011) and Tsvetkov et al. (2012). However, systematic offsets of 0.04–0.15 mag exist between the FLWO $u'BVr'i'$ data of SN 2011dh and the measurements reported by Arcavi et al. (2011) and Tsvetkov et al. (2012). The offsets are essentially constant for all phases and have values of $u' = -0.05$ mag, $B = +0.15$ mag, $V = +0.11$ mag, $r' = -0.04$ mag, and $i' = +0.08$ mag. Accounting for these offsets, the FLWO LCs match Arcavi et al. (2011, i'), Tsvetkov et al. (2012, $u'BVr'$), and Sahu et al. (2013, *UBVRI*) within ±0.05 mag. The FLWO data in Table 3 and Figure 3 are our measurements, and no offsets have been applied.

NIR images were obtained in the J, H, and K_s bands by the Peters Automated Infrared Imaging Telescope (PAIRITEL), a 1.3 m $f/13.5$ telescope located at the FLWO (Table 5). The data are processed into mosaics using the PAIRITEL Mosaic Pipeline version 3.6 implemented in Python. Details of PAIRITEL observations and reduction of SN data can be found in Friedman (2012).

UVOT photometric data were downloaded from the *Swift* archive (Table 6). *Swift* photometry is reduced with HEAsoft following standard procedures. Individual frames were summed with the `uvotimsum` task, and magnitudes were determined via aperture photometry using the task `uvotsource` with a 5 arcsec radius aperture. This sequence produces standard Johnson magnitudes in *UBV* filters and flight system magnitudes in *UVW2, UVM2*, and *UVW1*. The transmission profiles of the *UVW1* and *UVW2* filters have extended red wings that permit flux contributions from beyond the intended wavelength regions.

3. SPECTRA

The earliest spectrum in Figure 1 was obtained on June 4.2 UT, which is less than 4 days after the estimated time of the explosion. The final spectrum in our sample was obtained on

Table 3
Photometric Measurements with the FLWO 1.2 m and KeplerCam

Date (UT)[a]	u'	u'err	B	B err	V	V err	r'	r'err	i'	i'err
55716.2	15.676	0.012	15.115	0.011	14.692	0.010	14.534	0.015	14.759	0.020
55717.2	15.754	0.023	14.866	0.009	14.363	0.008	14.186	0.010	14.510	0.013
55718.2	15.563	0.016	14.580	0.009	14.056	0.009	13.924	0.012	14.242	0.017
55719.2	15.307	0.011	14.264	0.007	13.743	0.008	13.602	0.011	13.941	0.014
55721.1	14.971	0.154	13.849	0.006	13.305	0.010	13.165	0.016	13.543	0.020
55722.1	14.854	0.134	13.677	0.007	13.128	0.010	13.007	0.013	13.358	0.017
55723.2	...	...	13.549	0.011	13.018	0.011	12.899	0.013	13.208	0.013
55724.2	...	...	13.462	0.006	12.879	0.009	12.758	0.012	13.087	0.019
55725.2	...	...	13.397	0.006	12.788	0.009	12.650	0.012	12.981	0.015
55726.2	...	...	13.351	0.004	12.735	0.006	12.605	0.008	12.890	0.010
55727.2	...	...	13.295	0.006	12.667	0.008	12.525	0.013	12.814	0.017
55729.2	...	...	13.199	0.007	12.555	0.009	12.419	0.011	12.686	0.016
55730.2	...	...	...	...	12.514	0.008	12.391	0.010	12.634	0.012
55731.3	...	...	13.165	0.006	12.490	0.008	12.342	0.010	12.587	0.014
55732.1	14.456	0.008	13.164	0.009	12.463	0.008	12.311	0.011	12.537	0.015
55733.3	...	...	13.183	0.008	12.451	0.010	12.281	0.013	12.506	0.014
55734.2	14.578	0.006	13.211	0.004	12.456	0.005	12.282	0.006	12.481	0.007
55735.2	...	...	13.293	0.004	12.488	0.003	12.290	0.005	12.467	0.005
55736.2	14.877	0.010	13.386	0.008	12.515	0.010	12.315	0.011	12.495	0.014
55738.2	15.261	0.011	13.650	0.006	12.676	0.005	12.398	0.005	12.523	0.006
55739.2	15.510	0.011	13.810	0.005	12.773	0.004	12.482	0.007	12.571	0.007
55740.2	...	...	13.900	0.006	12.868	0.003	12.551	0.003	12.618	0.003
55742.2	16.059	0.018	14.236	0.009	13.069	0.010	12.687	0.011	12.727	0.016
55743.2	16.215	0.024	14.324	0.008	13.169	0.004	12.765	0.003	12.756	0.003
55744.2	16.443	0.026	14.474	0.008	13.249	0.006	12.829	0.008	12.818	0.010

Notes. Systematic offsets of $u' = -0.05$ mag, $B = +0.15$ mag, $V = +0.11$ mag, $r' = -0.04$ mag, and $i' = +0.08$ mag are found between the FLWO 1.2 m data and other published data (see Section 2.2). Accounting for these offsets, the FLWO light curves match Arcavi et al. (2011, i') and Tsvetkov et al. (2012, $u'BVr'$) within ± 0.05 mag.
[a] Average time of observation for a sequence with multiple filters. Estimated date of explosion: MJD = 55712.5.

Table 4
Sequence of Local Comparison Stars

ID	R.A. (J2000)	Decl. (J2000)	u'	u' err	B	B err	V	V err	r'	r' err	i'	i' err
A	13:30:21.93	+47:09:05.7	17.230	0.098	16.454	0.021	15.895	0.014	15.686	0.017	15.495	0.023
B	13:30:14.29	+47:14:56.0	17.922	0.110	16.918	0.021	16.295	0.012	16.052	0.016	15.839	0.018
C	13:30:13.86	+47:07:30.1	17.877	0.092	16.475	0.020	15.653	0.012	15.334	0.016	15.064	0.016

Note. Finding chart is displayed in Figure 4.

Table 5
Photometric Measurements with PAIRITEL

Date (UT)[a]	J	J err	H	H err	K_s	K_s err
55717.1	13.875	0.193	13.762	0.535	13.607	0.369
55718.2	13.624	0.153	13.473	0.401	13.497	0.341
55719.2	13.398	0.123	13.400	0.370	13.077	0.255
55720.2	13.196	0.100	13.154	0.292	13.027	0.296
55721.2	12.993	0.082	13.017	0.255	12.969	0.185
55722.2	12.821	0.068	12.807	0.205	12.702	0.151
55723.2	12.696	0.061	12.659	0.178	12.510	0.153
55724.2	12.585	0.055	12.532	0.155	12.317	0.122
55725.1	12.477	0.050	12.473	0.151	12.427	0.125
55726.2	12.377	0.054	12.375	0.148	...	...
55727.2	12.327	0.050	12.291	0.130	12.214	0.162
55728.2	12.230	0.044	12.140	0.119	12.047	0.156
55730.2	12.143	0.041	12.102	0.110	11.933	0.133
55731.2	12.105	0.038	12.016	0.097	12.,000	0.101
55732.2	12.039	0.036	12.045	0.105	11.934	0.108
55733.2	12.051	0.036	11.908	0.088	11.986	0.030
55734.2	11.868	0.081	11.868	0.077	11.976	0.039
55735.2	11.898	0.099	11.931	0.217	11.931	0.217

Note. [a] Average time of observation for a sequence with multiple filters. Estimated date of explosion: MJD = 55712.5.

July 4, which is 34 days after the explosion. Observing details for each spectrum are given in Table 1. The wavelengths of lines, features, or spectra are expressed in angstroms for wavelengths less than 8000 Å and in microns for wavelengths greater than or equal to 0.80 μm. When a discussion includes wavelengths that cross 8000 Å, all wavelengths are expressed in the same units. The times of observation are expressed in whole days relative to the explosion. As a point of reference, the B-band maximum occurred about 20 days after the explosion.

Figure 2 displays optical and NIR spectra from SN 2011dh covering the wavelength region 0.32–2.40 μm. The NIR data were obtained at the IRTF with SpeX on days 8, 12, and 16, while the corresponding optical data were obtained at the FLWO with FAST on day 8 and the HET with LRS on days 11 and 17. Blackbody (BB) temperature curves are plotted as dotted lines in Figure 2. The observed shapes of the optical and NIR continua are fit best by BB curves for 8500 K at 8 days, 8400 K at 12 days, and 8100 K at 16 days. A more detailed discussion of temperature estimates can be found in Section 8.

Figure 1 shows that the *HST*/STIS spectrum obtained on day 24 extends from 2100 to 10000 Å, although the portion beyond 9000 Å suffers from fringing. Features of Ca II H&K

Table 6
Photometric Measurements with *Swift*

Date (UT)[a]	*UVW2*	*W2* err	*UVM2*	*M2* err	*UVW1*	*W1* err	*U*	*U* err
55716.0	16.31	0.03	15.94	0.03	15.40	0.02	14.95	0.02
55716.7	16.61	0.05	16.19	0.05	15.56	0.03	15.09	0.02
55717.7	16.83	0.07	16.51	0.08	15.81	0.05	15.14	0.03
55719.0	16.74	0.06	16.70	0.04	15.86	0.04	14.88	0.02
55720.6	17.00	0.14	16.84	0.17	15.76	0.04	14.47	0.02
55721.8	16.80	0.08	17.19	0.11	15.68	0.03	14.28	0.02
55723.1	16.93	0.13	17.23	0.13	15.59	0.03	14.14	0.02
55723.8	16.78	0.14	17.38	0.17	15.67	0.05	14.07	0.02
55725.1	16.89	0.05	17.16	0.08	15.63	0.03	13.99	0.02
55726.6	16.98	0.05	17.60	0.12	15.59	0.03	14.01	0.02
55728.8	16.97	0.10	17.66	0.16	15.60	0.06	13.93	0.05
55729.2	16.86	0.10	17.42	0.14	15.61	0.06	13.87	0.05
55730.3	16.80	0.08	17.41	0.11	15.56	0.06	13.89	0.05
55731.5	16.89	0.10	17.62	0.16	15.53	0.06	13.91	0.05
55732.5	16.89	0.08	17.66	0.12	15.63	0.06	13.93	0.05
55733.5	17.01	0.09	17.67	0.13	15.64	0.06	13.99	0.05
55734.4	17.03	0.09	17.59	0.13	15.70	0.06	14.08	0.05
55735.7	16.97	0.09	17.81	0.15	15.82	0.07	14.25	0.05
55736.2	17.17	0.10	17.96	0.18	15.84	0.07	14.31	0.05
55737.2	17.45	0.12	17.80	0.20	16.03	0.08	14.56	0.05
55738.8	17.39	0.09	17.79	0.31	16.24	0.05	14.82	0.03
55740.2	17.70	0.13	18.77	0.58	16.51	0.05	15.13	0.03
55741.4	17.77	0.15	18.29	0.26	16.67	0.08	15.34	0.04
55741.8	17.89	0.15	18.43	0.25	16.66	0.07	15.49	0.04
55743.8	18.47	0.26	19.15	0.51	17.10	0.11	15.90	0.05
55745.2	18.11	0.19	18.95	0.41	17.02	0.10	16.02	0.06
55746.1	18.54	0.27	18.32	0.22	17.31	0.12	16.18	0.06

Note. [a] Average time of observation for a sequence with multiple filters. Estimated date of explosion: MJD = 55712.5.

λ3945 and the Ca II infrared triplet λ8579 are both observed in a single spectrum. At other phases, it is necessary to combine spectra from multiple sources to cover this range. The optical portion of the STIS spectrum is in good agreement with a FAST spectrum obtained on the same date and with the HET spectrum obtained on day 22.

A unique part of the *HST* spectrum is the UV coverage. Figure 5 shows the 2000–4200 Å region of the *HST*/STIS spectrum from SN 2011dh on day 24, plotted with STIS spectra of SN IIb 1993J (Jeffery et al. 1994) and 2001ig at comparable phases. The flux from SN 2011dh is clearly suppressed below 3300 Å relative to the other SN IIb. Fe II, Ti II, and Cr II are expected to be strong contributors to the UV spectrum, and these lines can create a line-blanketing effect that shifts flux from the UV to longer wavelengths. In Section 5, we analyze the UV region of this spectrum using model spectra from SYNOW. The spectrum of SN 2001ig is from the *HST* archives and has not been previously published.

3.1. Hydrogen Features

Silverman et al. (2011) reported that a Keck I+LRIS spectrum of SN 2011dh obtained on day 3 revealed P Cygni profiles for hydrogen lines that are characteristic of Type II SNe. The data in our sample begin the following day. Figure 6 displays the strongest H I features by phase in velocity space. Figure 6 shows that H I features are strongest in the earliest observations, and they become progressively weaker and narrower with time. Hα is the only H I line that continues to form a significant absorption by the end of these observations, 34 days after the explosion.

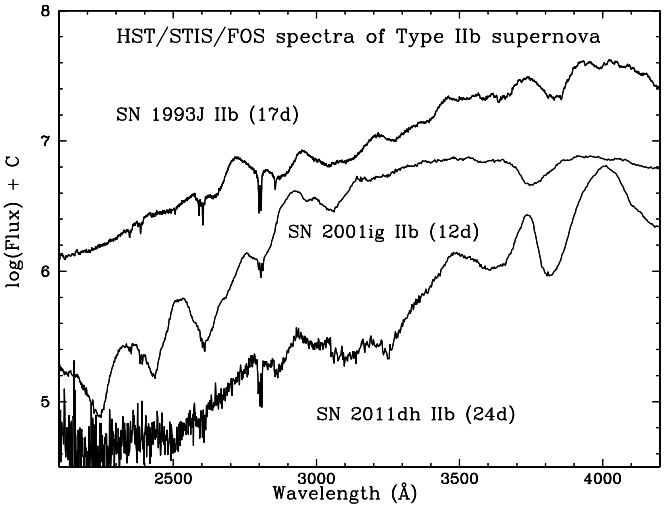

Figure 5. *HST*/STIS data from three Type IIb SN. The spectra are displayed from 2000 to 4200 Å to show detail in the UV region. The SN 2011dh spectrum obtained on day 24 (bottom) reveals a reduced UV flux at wavelengths less than 3300 Å compared to spectra from SN IIb 2001ig on day 12 (middle) and SN IIb 1993J on day 17 (top). We model this region with SYNOW (Section 5), and the results suggest that the UV suppression is due to line blanketing from Ti II and Co II.

Maund et al. (2011) report that the transition from H-dominated spectra to He is nearly complete 40 days after the explosion.

In the first 2 weeks after the explosion, Hα line profiles show possible evidence for two separate absorption components. At day 4, the Hα absorption feature can be fit by two Gaussians with minima that correspond to velocities of 17,300 and 15,400 km s^{-1}. Silverman et al. (2011) reported the Hα velocity on day 3 to be 17,600 km s^{-1}, which suggests that they measured the blue component. Figure 6 shows the development of the Hα feature by phase. The component on the red side of the double bottom becomes dominant after day 8, and by day 24 it provides the only minimum for the Hα line profile. For consistency, we measure Hα velocities using the red component at all phases.

The source of the blue component in the Hα features is ambiguous. One possibility is a second H-rich region with a velocity about 2000 km s^{-1} higher. No comparable high-velocity (HV) components are found in the absorption features from other H I lines, but they could be disguised by blending. SYNOW models suggest this is a possibility. The addition of a second H region to SYNOW models can fit the observed "double" Hα line profiles without producing strong HV features for other H I lines. An outer H layer could also be created by interaction with circumstellar material as described by Chugai et al. (2007).

Si II λ6355 is another possibility for the source of the blue absorption component in Hα, but that identification requires the Si II velocities to be 5000 km s^{-1} lower than Ca II and 4000 km s^{-1} lower than Fe II at these early phases. Those velocities seem unlikely, although SYNOW models can produce features that match the observed Hα line profiles using Si II for the blue component.

Figure 6 shows that line profiles for most H I features are distorted by the influence of other lines that are gaining strength with time while H I is fading. Hβ velocities follow the general shape of the Hα velocity curve with values about 1500 km s^{-1} lower than Hα. Hβ is distorted on the red side by P Cygni emission from a strong blend of Mg II λ4481 and Fe II λ4561. Figure 6 shows how the Hβ feature is shoved to

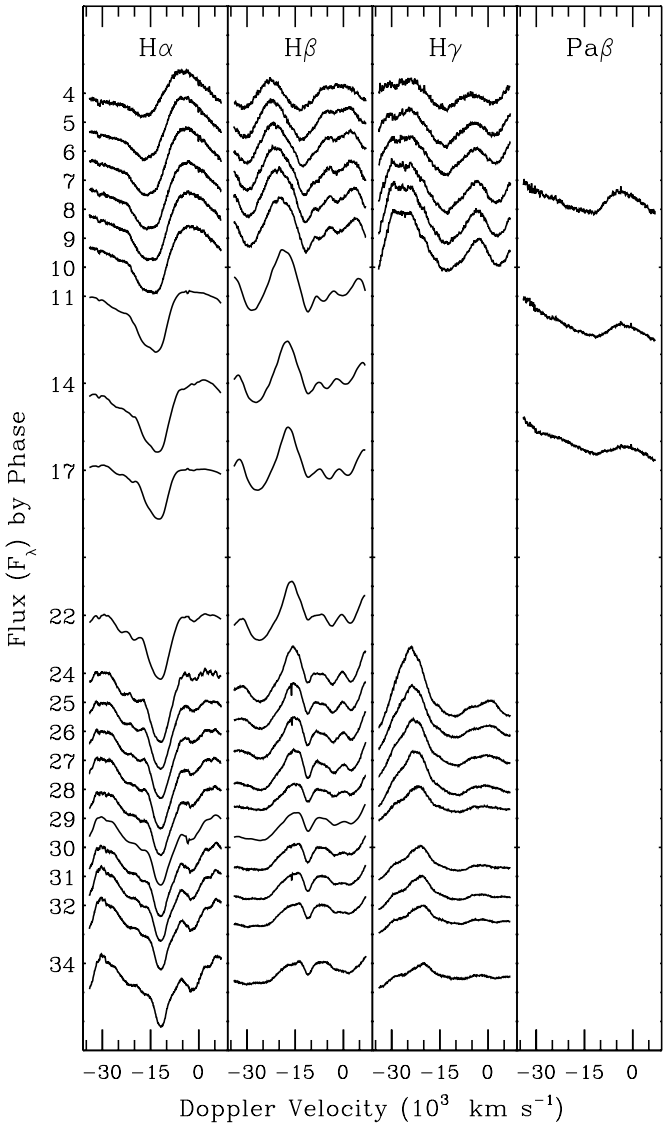

Figure 6. Hydrogen features by phase in velocity space. All H I features are strongest in the first spectra, and they become weaker and narrower with time. The Hα velocity is 15,400 km s^{-1} on day 4 and declines to about 12,500 km s^{-1} on day 14. From day 14 to day 34, the Hα velocity remains nearly constant at about 12,000 km s^{-1}. Section 3.1 describes distortions and blends that affect each H I line as H weakens and other lines become stronger. Flux values for Paβ are multiplied by 5 to facilitate comparison. Velocities are listed in Table 7.

longer wavelengths, which results in lower measured velocities for Hβ. After maximum brightness, He I λ4492 produces the same effect on Hβ.

Hγ is squeezed by Ca II H&K emission on the blue side and by the Mg II λ4481 and Fe II λ4561 feature on the red side. Our data do not cover the Hγ region between days 11 and 24, and it is not possible to identify Hγ in the spectra after day 24.

Paα λ1.8751 is located in a wavelength region with high atmospheric opacity. In Figure 2, we follow standard practice for displaying NIR spectra and omit the wavelength regions where the atmospheric transmission is less than 50% (1.32–1.38 and 1.79–1.88 μm). After those data have been removed, the only information we have about the Paα line profile is the extreme red tail of the emission component.

The H I line that is most free from blending is Paβ λ1.2818. Features from this line are displayed in the rightmost panel of Figure 6, and they show that the strength of the H I signal is clearly diminishing from day 8 through day 16. Unfortunately, our NIR spectra cover only a limited range of dates.

3.2. Helium Features

The presence of helium in the spectra of SN IIb differentiates them from other Type II SN, but classification is only one reason to search for helium. The development of He I features provides information about the transition in SN IIb from a hydrogen-dominated epoch soon after the explosion to the later phases dominated by helium. NIR spectra provide the most reliable detections of He I features in early observations of SN because optical He I lines other than λ5876 are weak or blended. Figure 2 shows that He I lines at optical wavelengths are difficult to identify in the early data (see also the discussions of He I lines in SN 2008ax by Chornock et al. 2011 and by Taubenberger et al. 2011).

Evidence from the λ1.0830 line in isolation is insufficient to confirm the presence of He I (besides the fact that it violates the admonition in the previous paragraph). A broad absorption feature from about 1.02 to 1.06 μm is found in the spectra of most core-collapse SN, including SN Ic, which never display clear evidence for He I. Paγ λ1.0938, He I λ1.0830, and Fe II λ1.0500 are usually the most prominent contributors to this feature. Several other strong lines are found in this region, and a combination of them is likely to help form the line profile. Good candidates include C I λ1.0603, Mg II λ1.0927, Si I $\lambda\lambda$1.0608,1.0962, S I λ1.0457, Fe II λ1.0863, and Ti II λ1.0691, but it is often difficult to define specific minima and associate them with individual lines.

He I lines are marked in Figure 2 at 8000 km s^{-1}. Eight days after the explosion (the top spectrum) no He I features are detected. At 11 and 12 days (middle), He I $\lambda\lambda$5876,1.0830 features are evident, while λ 2.0581 is weak. Taken together, these features show that helium is present 11 days after the explosion, but separately, the features would not be convincing detections due to blends with Na I λ5892 and Paγ λ1.2818, respectively. The spectra obtained on days 16 and 17 reveal unambiguous features of He I from λ5876 and both strong NIR lines $\lambda\lambda$ 1.0830, 2.0581, as described in Marion et al. (2011).

In Figure 2, Paγ and He I λ1.0830 are positioned within 100 km s^{-1} of each other due to the velocity difference between the blueshifts for H I and He I. Paγ dominates the red component of the 1.02–1.06 μm feature on day 8, and all H I lines are strong at this phase. On day 12, the red end of the feature has developed more of a P Cygni profile as He I λ1.0830 begins to influence the line profile, but Paγ remains strong. Fe II λ1.0500 probably forms the absorption at the blue end of this feature at all phases.

The absorption feature for He I λ2.0581 is pushed to the red by the strong emission component of the Paα P Cygni profile that is mostly hidden in the high-opacity region that we omit from the spectra.

Figure 7 displays features for three optical and two NIR He I lines by phase in velocity space. Other He I lines begin to emerge on about day 17, which is near the time of *B* max, and all He I features become deeper and broader with time. In the early spectra He I λ3889 is blended or obscured by Ca II H&K and Si II λ3858. After *B* max, He I λ3889 is strong enough to distort the Ca II H&K feature by extending it on the blue side, but accurate measurement of the He I contribution is not possible. He I λ4492 is blended with Fe II λ4561 and Mg II λ4481, and it is not possible to unravel the He I contribution from the blend. He I λ5016 is blended with Fe II λ5018 at all phases covered by these data. He I λ6678 begins to flatten the emission component

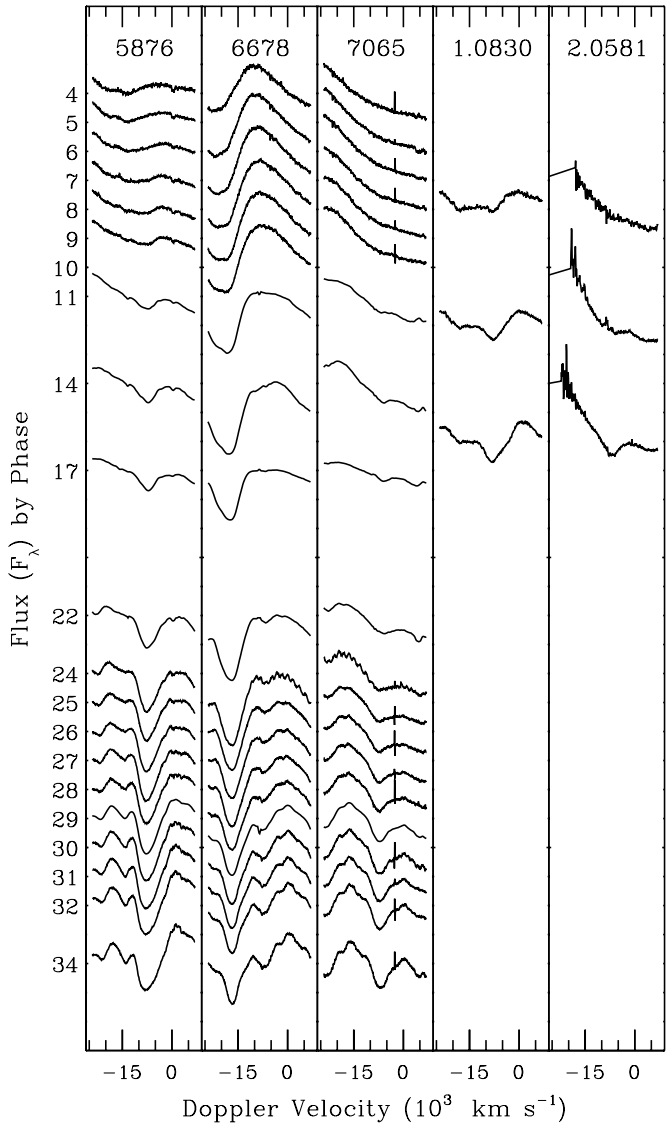

Figure 7. He I features by phase in velocity space. Helium is not detected until 11 days after the explosion when features of He I λ5876 and λ1.0830 (day 12) confirm the presence of He I (see also Figure 2). He I features progressively strengthen through the time covered by these observations, and velocities are nearly constant from day 14 to day 34. Weaker lines such as λ6678 are not clearly detected until day 22. Flux for the λ2.0581 feature is multiplied by 10 to facilitate comparison. Velocities are listed in Table 7.

of Hα on day 14, but contributions from this line are obscured by Hα emission until 22 days after the explosion. He I λ7065 is weak in spectra from days 14 and 17, but because this line is relatively unblended, it provides a reliable benchmark for He I velocities at all phases. Table 7 shows that the velocities for all He I lines are within 1000 km s^{-1} of He I λ7065 after day 24 when He I has become established.

3.3. Ca II and Fe II Features

Ca II and Fe II are the only unambiguous identifications in the spectra of SN 2011dh other than H I and He I.

Ca II is clearly detected from both the infrared triplet (IR3, λ0.8579) and Ca II H&K (λ3945). These strong lines create broad absorption features with rounded bottoms, which makes it difficult to identify distinct absorption minima. Ca II does not appear to have separate contributions from two absorption regions as found in the early Hα features. To measure the Ca II features, we define a straight-line continuum between the flux at specific wavelengths on both sides of each feature. Because the bottom of the line profile is a broad curve, small changes in the position of the assumed continua due to noise or imperfect telluric removals can create differences up to 2000 km s^{-1} in the positions of the minima of these features. Consequently, velocity uncertainties for Ca II are greater than for velocities measured from narrow features. By using a consistent measurement technique, we provide a satisfactory description of the behavior of Ca II velocities in the spectra from SN 2011dh.

On days 6 and 11, the IR3 profile is similar to the combined profile of HV and photospheric Ca II that is often seen in early spectra from Type Ia SNe (Mazzali et al. 2005). However, it is not possible to clearly define separate minima in the IR3 feature, and Ca II H&K displays no evidence for a HV component at these epochs. After day 17, the profile of the Ca II IR3 feature becomes asymmetrical, and the blue side has a steeper gradient than the red side. The Ca II H&K feature becomes stronger from the first observation on day 4 through day 11. This is followed by a gap in our coverage of this wavelength region from day 12 to day 23. On day 24, Ca II H&K is still strong, but the feature declines after day 27 and is very weak by day 34. Ca II H&K is likely to be blended with Si II λ3858 and He I λ3889.

Fe II becomes stronger from the earliest observations through day 14 and then slowly declines. The λ5169 line is most frequently used to represent Fe II velocity in SN IIb (Taubenberger et al. 2011). An absorption feature from this line is detected in all optical spectra in our sample. Unlike H I and He I, for which the velocity remains nearly constant after day 17, the Fe II velocity steadily declines through the entire time period covered by our observations. Fe II λ4561 blends with Mg II λ4481 to create a strong absorption feature in the early spectra. This feature becomes stronger but even less defined when He I λ4492 begins to contribute about day 17. Fe II λ5018 is distinct on days 4–14. This line is subsequently blended with He I λ5016 and eventually obscured as the helium lines become stronger. Fe II λ1.0500 is present and measured in all of the NIR spectra.

3.4. Other Features

The following ions show hints of absorption features from some of their stronger lines. We discuss the most likely identifications.

O I is not detected through day 17 but may be emerging in the day 22 and 29 spectra from the λ7773 O I line. The absorption feature found near 0.90 μm in the NIR spectra on days 8, 12, and 16 is not primarily due to O I λ0.9264 because the stronger O I λ7773 line is not detected before day 22.

Mg II is likely to be present in the NIR spectra from the λ0.9227 line that contributes to the strong absorption near 0.9 μm in a blend with O I λ0.9264 and Si II λ0.9413. Mg II λ1.0927 is a part of the broad absorption feature from 1.01 to 1.06 μm, but no individual lines are identified in this blend other than Paγ, He I λ1.0830, and Fe II λ1.0500. Mg II λ4481 definitely contributes to the absorption feature found near 4350 Å in a blend with Fe II λ4561. The minimum of this feature corresponds to less than 7000 km s^{-1} for Mg II, which is inconsistent with the velocities of other intermediate-mass elements. This suggests that the 4350 Å absorption feature is dominated by Fe II early and He I λ4492 after day 17.

Si II does not produce obvious absorption features. Si II λ6355 may contribute to the Hα double feature

Table 7
Velocity Measurements of H and He Lines (km s^{-1})

Epoch[a]	Hα	Hβ	Hγ	Paβ	He I 5876	He I 6678	He I 7065	He I 1.0830	He I 2.0581
4	15400	13800	14100	...	...	...	...	...	...
5	14500	13,000	13900	...	...	...	...	...	...
6	14100	12700	13600	...	...	...	...	...	...
7	13700	12200	13500	...	...	...	...	...	...
8	13500	12,000	13400	...	...	...	...	...	...
9	13300	11600	13100	...	...	...	...	...	...
10	...	...	12600	...	...	...	...	...	...
11	13100	11,000	12500	...	8400	...	...	...	...
12	...	...	...	12200	...	...	...	8200	...
13	...	...	...	...	...	...	...	...	...
14	12500	10800	...	...	7600	...	...	...	...
15	...	...	...	12,000	...	...	...	...	...
16	...	...	...	...	...	...	...	8,000	7200
17	12400	10700	...	...	7500	...	...	...	...
18	...	...	...	11900	...	...	...	...	...
19	...	...	...	...	...	...	...	...	...
20	...	...	...	...	...	...	...	...	...
21	...	...	...	...	...	...	...	...	...
22	12100	10600	...	...	7500	6500	...	...	...
23	...	...	...	...	...	...	...	...	...
24	12100	10900	...	...	7600	6600	7400	...	...
25	11900	11,000	...	...	7400	6600	7200	...	...
26	12100	11,000	...	...	7600	6900	7200	...	...
27	12,000	10800	...	...	7600	7100	7100	...	...
28	11900	10800	...	...	7500	7200	7100	...	...
29	12,000	10700	...	...	7400	7600	7,000	...	...
30	12,000	10900	...	...	7500	7300	6900	...	...
31	12,000	10900	...	...	7600	7300	7,000	...	...
32	11900	10800	...	...	7700	7200	7,000	...	...
33	...	...	...	...	...	...	...	...	...
34	11800	10800	...	...	7800	7100	6800	...	...

Note. [a] Whole days with respect to the time of explosion.

(Section 3.1). However, the minima of the blue components correspond to Si II λ6355 velocities of 8500 km s^{-1} on day 4 and less than 8000 km s^{-1} on days 8–10. Those velocities are more than 4000 km s^{-1} less than for any other lines measured during these phases. Si II λ3858 may influence the blue side of the Ca II H&K feature, but detection is not possible. Si II λ4130 is a candidate for the flat top and slight absorption in the Ca II H&K emission component found near 3950 Å in the early spectra. However, the velocities required are greater than observed for Hα. In the NIR, Si II λ0.9413 may contribute to the 0.9 μm feature in a blend with Mg II λ0.9227. The small absorption features in the *H* band at about 1.65 μm on days 12 and 16 could be from Si II λ1.6930.

Ti II and Co II are the likely source of the steep drop of the continuum flux below 3300 Å due to line blanketing (Figure 5). Unlike SN 2001ig, there are no distinct absorption features in this region that can be associated with individual lines, but SYNOW model spectra (Section 5) require significant contributions from Ti II and Co II to match the reduction of the UV continuum level observed in early spectra from SN 2011dh.

4. VELOCITY MEASUREMENTS

Velocity measurements for H I, He I, Ca II, and Fe II are plotted by phase in Figure 8, and they are listed in Tables 7 and 8. The symbol shapes correspond to the ions: circles = H I, squares = He I, diamonds = Ca II, and triangles = Fe II. The different lines for each ion are represented by different colors. Open symbols (Hβ and Ca II) indicate greater uncertainties in the velocity measurements.

All velocities decline rapidly from the first detection through the time that He I appears (marked at 11 days on Figure 8). A more gradual rate of decline follows until the time of *B* max at day 20. After maximum brightness, H I and He I velocities remain constant, while Ca II and Fe II velocities continue to decline.

Beginning on about day 24, Ca II velocities move away from the H-layer velocities toward the lower He-layer velocities. Fe II velocities decline at a nearly constant rate throughout the entire period covered by these observations except for an abrupt drop from about day 9 to day 12. This break may be due to an opacity effect because it occurs at about the same time that we begin to see evidence for He I. After day 22, Fe II velocities do not become constant, like H I and He I, but they continue to decline through the end of our observations. Fe II velocities separate from H I velocities about two weeks earlier than Ca II velocities make the same transition. The relative velocities between ions we find for SN 2011dh are similar to those reported for SN 2008ax by Taubenberger et al. (2011).

4.1. Separate Line-forming Regions for H and He

Figure 8 makes it easy to see that H I and He I velocities in SN 2011dh maintain a nearly constant separation of about 4000 km s^{-1} during the period in which both ions are detected.

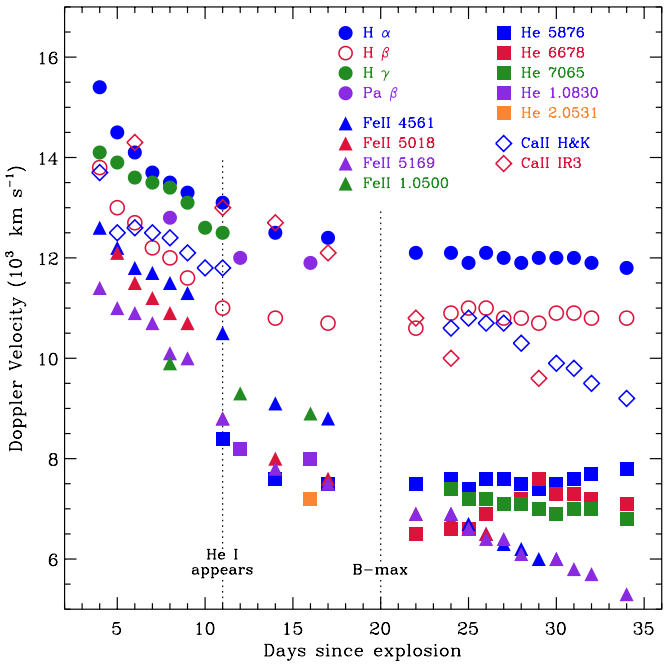

Figure 8. Velocities of H I, He I, Ca II, and Fe II plotted by phase. Each ion has its own symbol, and each line is a different color. All velocities decline rapidly until about day 11, when He I is first detected. H I and He I velocities are nearly constant after *B* max, while Ca II and Fe II continue to decline. The gap between the H I velocities (circles) and He I velocities (squares) is ≈4000 km s^{-1} at all phases. The open symbols indicate features for which there is increased uncertainty in the velocity measurements (see Sections 3.2 and 3.3). Values used in the figure are listed in Tables 7 and 8.

(A color version of this figure is available in the online journal.)

Table 8
Velocity Measurements of Ca II and Fe II Lines (km s^{-1})

Epoch[a]	Ca II 3945	Ca II 8579	Fe II 4561	Fe II 5018	Fe II 5169	Fe II 1500
4	13700	···	12700	···	11400	···
5	12500	···	12300	12200	11,000	···
6	12600	14300	11800	11500	10900	···
7	12500	···	11700	11200	10700	···
8	12400	···	11900	10900	10100	9500
9	12100	···	11400	10700	10000	···
10	11800	···	···	···	···	···
11	11800	13,000	10500	8800	8800	···
12	···	···	···	···	···	9100
13	···	···	···	···	···	···
14	···	12700	8900	8,000	7800	···
15	···	···	···	···	···	···
16	···	···	···	···	···	8700
17	···	12100	8800	7600	7500	···
18	···	···	···	···	···	···
19	···	···	···	···	···	···
20	···	···	···	···	···	···
21	···	···	···	···	···	···
22	···	10800	8200	6900	6900	···
23	···	···	···	···	···	···
24	10600	10000	7500	6800	6900	···
25	10800	···	7300	6600	6600	···
26	10700	···	6900	6500	6400	···
27	10700	···	···	···	6400	···
28	10300	···	···	···	6100	···
29	···	9600	···	···	···	···
30	9900	···	···	···	6,000	···
31	9800	···	···	···	5800	···
32	9500	···	···	···	5700	···
33	···	···	···	···	···	···
34	9200	···	···	···	5300	···

Note. [a] Whole days with respect to the time of explosion.

The detection of both H I and He I at the same phase but at different velocities was discussed by Branch et al. (2002) for SN Ib. They use SYNOW models with a detached hydrogen component at 13,000 km s^{-1} and a helium region at 9000 km s^{-1} to fit spectra of SN Ib obtained near *B* max. Models for SN IIb by Dessart et al. (2011) match our observations of the relative strengths of H and He features by phase. They also predict that hydrogen velocities will always exceed helium velocities. Previous observations of separated velocities for hydrogen and helium have been reported for SN IIb 2008ax (Chornock et al. 2011) and SN IIb/Ib 2011ei (Milisavljevic et al. 2013).

Figure 9 presents another way to view the velocity relationship between the H and He regions. He I λ5876 (left column, blue) and Hα (center, red) are plotted by phase and in velocity space with the same relative flux scale. He I is absent or very weak at early times, and it is blended with Na D. The first detection of He I is on day 11 (Section 3.2), and Figure 9 shows that He I features become progressively stronger while H I features weaken.

The right panel shows the H I and He I features plotted together with their line depths normalized to the same value. Generally, similar line profiles are observed for the first few days, but this is a coincidence with the Hα profile that has a double minimum and the He I profile that is strongly blended with Na D and has been magnified by the normalization.

The minima of the features from Hα and He I λ5876 are obviously separated from day 11 when He I first develops a defined minimum. From day 11 to day 22 the velocities for both lines decline slightly, but the separation between them remains essentially constant. From day 22 to day 34 the velocities for both lines are nearly constant.

These velocity measurements provide evidence that H lines are formed in a region that is expanding ≈4000 km s^{-1} faster than the layer in which He lines are produced. This separation is consistent with a model in which the progenitor explodes inside a hydrogen-rich shell. In the first days after the explosion, H-shell opacity conceals all of the material inside the shell. Opacity in the shell region is diluted by expansion of the SN, and when the H layer becomes optically thin, the helium-rich regions below are exposed. In SN 2011dh this happens on about day 11. Milisavljevic et al. (2013) also use H and He velocities to suggest that the progenitor of SN 2011ei retained a hydrogen envelope at the time of explosion.

4.2. Mass of the Hydrogen Envelope

Velocity measurements of H I and He I in Type IIb SNe 2011dh, 2008ax, and 1993J provide enough information to compare the relative masses of the high-velocity, hydrogen-rich shells that surrounded the progenitors. From a basic formula for the optical depth of the hydrogen layer, we derive a simple model for the mass of the hydrogen shell. We assume that the first detection of He I features occurs when the surrounding H-rich layer becomes optically thin. Therefore,

$$\tau_{\rm H} = 1 = \kappa_T \times \rho \times dR, \quad (1)$$

where κ_T is the electron scattering opacity, ρ is the density, and dR is the thickness of the H layer. We also assume homologous expansion for the SN, so $R \sim v_{\rm H} \times t_{\rm He}$. The density is taken to

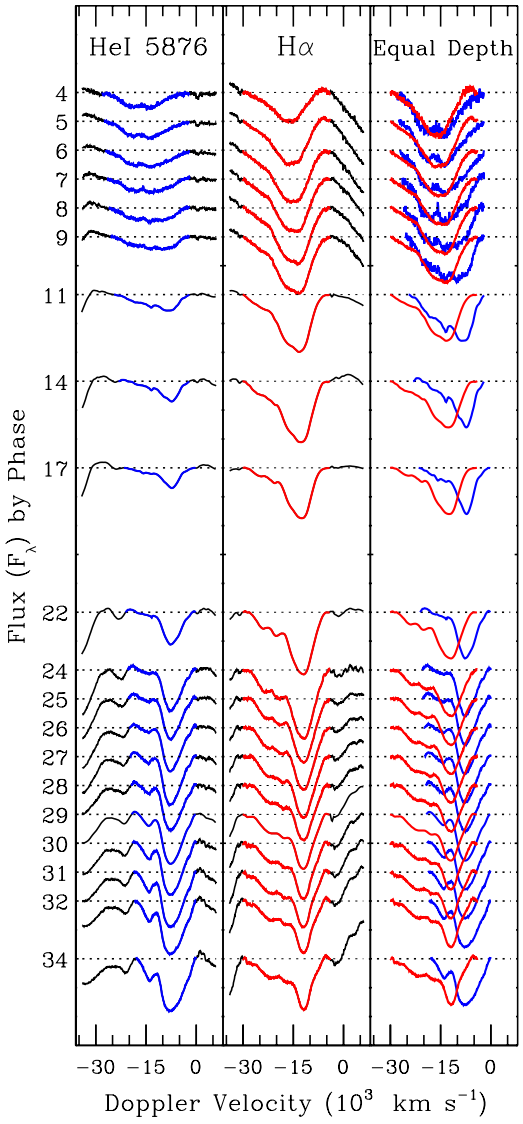

Figure 9. He I λ5896 (left, blue) and Hα (middle, red) normalized to a flat continuum and plotted in velocity space. The left and center panels have the same relative flux scaling. He I becomes progressively stronger from day 11 through the end of our data. Hα is strong early and becomes weaker and narrower with time. The right panel shows H I and He I plotted together with the line depths for both features normalized to the same value for comparison. By the time He I develops a clearly defined minimum on day 11, the H I and He I velocities are separated by about 4000 km s^{-1}. The velocity gap remains essentially constant from day 11 to day 34.

(A color version of this figure is available in the online journal.)

be constant, and we make a substitution: $\rho \propto M/R^3$. Then we obtain

$$M_{\rm H} \propto (v_{\rm H} \times t_{\rm He})^2, \quad (2)$$

where $v_{\rm H}$ is the velocity of the outer edge of the hydrogen shell and $t_{\rm He}$ is the time after the explosion when the He layer is first observed. Thus, $t_{\rm He}$ represents the time when the optical depth in H envelope reaches $\tau = 1$.

For all three of the SN IIb, the blue edge of the Hα absorption feature at the time of the first He I measurements is ≈20,000 km s^{-1}. If we accept $v_{\rm H}$ as a constant, then the mass of the hydrogen-rich shell is directly proportional to the square of the time from explosion to helium detection.

We have shown that for SN 2011dh, $t_{\rm He} \approx 11$ days, and from the literature we find for SN 2008ax $t_{\rm He} \approx 4$ days (Chornock et al. 2011; Taubenberger et al. 2011) and for SN 1993J $t_{\rm He} \approx$ 18 days (Barbon et al. 1995). These values for $t_{\rm He}$ indicate that the mass of the hydrogen shell surrounding the progenitor of SN 2011dh must be between the masses of the shells for SN 2008ax and 1993J.

Using Equation (2), we calculate

$$M_{\rm H}(\text{SN 2011dh}) \approx 8 \times M_{\rm H}(\text{SN 2008ax})$$

$$M_{\rm H}(\text{SN 2011dh}) \approx 0.3 \times M_{\rm H}(\text{SN 1993J}).$$

Supporting evidence is provided by the times required for the luminosity to decline from the initial shock-heated maximum to the minimum between the thermal and radiation peaks. As for the time of He I detection, the time of the LC minimum for SN 2011dh is between the other SN IIb. The time to minimum is ≈4 days for SN 2011dh, ≈1 day for SN 2008ax (Chornock et al. 2011; Taubenberger et al. 2011), and ≈9 days for SN 1993J (Richmond et al. 1994, 1996).

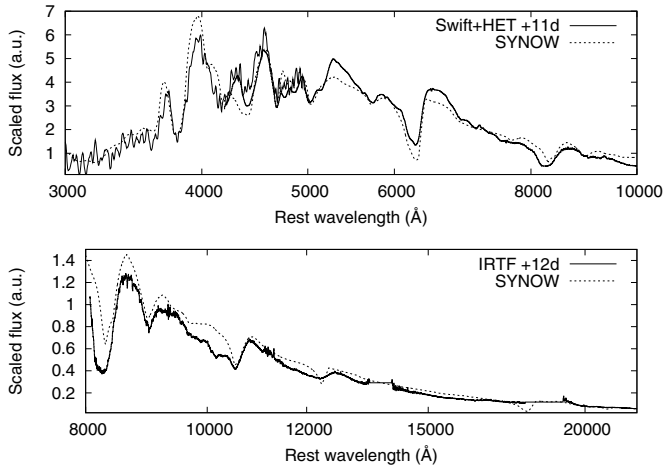

Figure 10. SYNOW model spectrum (dashed line) and a combined *Swift*/HET/IRTF spectrum (solid line) from days 11 and 12. The top panel shows the UV-optical region (3000–10000 Å), while the bottom panel shows the NIR (0.8–2.2 μm) with an overlap of ≈2000 Å. A detailed discussion of SYNOW modeling is given in Section 5.

5. MODEL SPECTRA

Figure 10 shows the combined *Swift*/HET/IRTF spectrum of SN 2011dh (solid line) obtained 11 and 12 days after the explosion plotted with a model spectrum covering 0.3–2.2 μm (dashed line) created with the parameterized modeling code SYNOW (Branch et al. 2003).

The SYNOW model successfully fits the shape of the continuum and accounts for the presence of most spectral features. The optical depth profile is assumed to be a function of velocity: $\tau = \tau(v_{\rm min}) \times (v/v_{\rm min})^{-n}$, where $v_{\rm min}$ is the minimum velocity for a given ion. The following ions (with their reference optical depths) are included in the model: H I (10), He I (0.2), Mg II (0.7), Si II (1), Ca II (50), Ti II (1), Fe II (1), and Co II (1).

The best SYNOW fit to the complete optical and NIR spectrum is achieved with a power-law index of $n = 6$, a temperature of $T_{\rm BB} = 9000$ K, the velocity of H lines at $v_{\rm phot} = 12,000$ km s^{-1}, and the velocities of all other lines at $v_{\rm phot} = 9000$ km s^{-1}. These are parameters for a simple line-fitting model and should not be considered physically precise. However, the SYNOW results clearly imply that the H line-forming region is located at a higher expansion velocity than

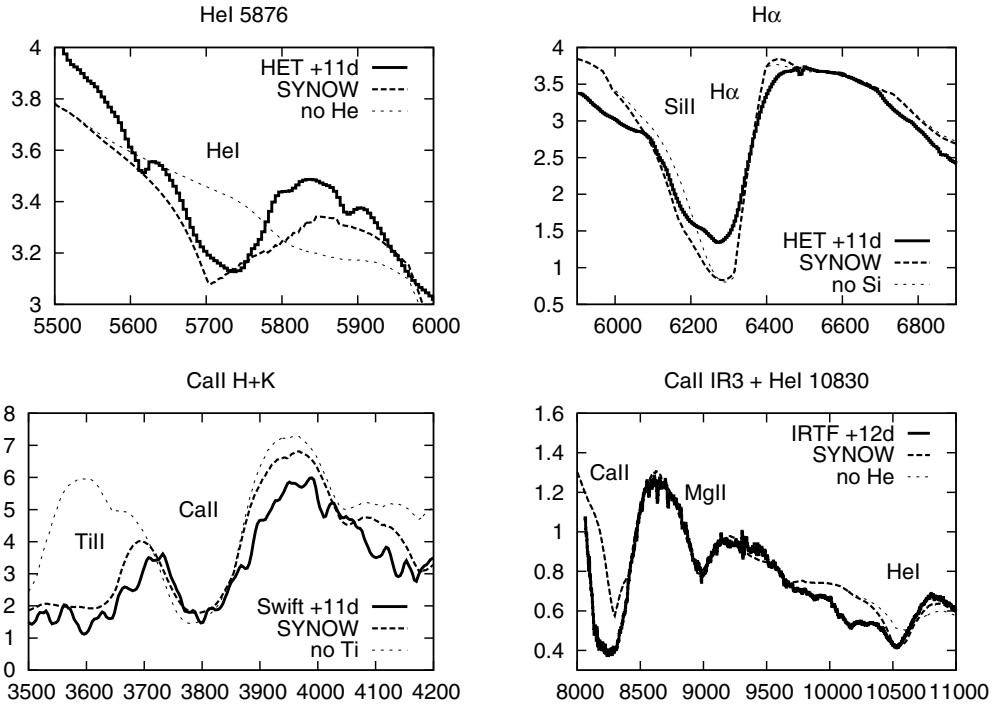

Figure 11. SYNOW model (dashed line) and the optical and NIR data from Figure 10 with each panel zoomed in on specific spectral features: He I λ5876 (top left), Hα (top right), Ca II H&K (bottom left), and Ca II IR3 plus He I λ1.0830 (bottom right). A comparison spectrum from which specific ions have been removed is plotted as the dotted line in each panel: He I is omitted in the top left and lower right panels, Si II is omitted in the upper right, and Ti II and Co II are omitted in the lower left. In each case, the fit with the dashed line is better than the fit with the dotted line. A detailed discussion of SYNOW modeling is given in Section 5.

the region forming the other lines. This is consistent with the observed separation of H I and He I velocities described in Section 4.1.

5.1. Early Evidence for He I

SYNOW models can help determine when He I becomes present in the spectra of SN 2011dh. He I detections on day 11 have been discussed, and we seek confirmation from the models for these identifications. Figure 11 zooms in on individual features to facilitate a detailed comparison of the model to the data.

The top left panel shows that the weak absorption feature near 5750 Å (solid line) is most accurately modeled (dashed line) when He I is included with a low optical depth (0.2). Note that the flux scale in this panel makes the feature appear stronger than it actually is relative to the other features in Figure 11. The model does not reproduce the line profile exactly, but it matches the size and location of the feature. The dotted line shows that a model without He I generates a poor fit to the data. The lower right panel of Figure 11 shows that the feature observed near 10500 Å in the day 12 data (solid line) is primarily due to Paγ (dotted line). However, the model fits the data better when He I is included (dashed line).

Thus, the SYNOW models suggest that He I is present 11 days after the explosion even though He I does not produce strong absorption features at this phase. Model results are not detections, but when they are consistent with the observational evidence (Section 3.2), they reinforce the identifications of features such as He I λλ5876, 1.0830 in the day 11 and 12 spectra.

5.2. Hα Features with Two Components

We use SYNOW to explore the double bottom found in the Hα profile of early spectra from SN 2011dh. The Hα feature is displayed in the upper right panel of Figure 11. The data (solid line) show that the blue component on day 11 is weaker than found in earlier data but still forms a distinct notch in the blue side of the profile. The dashed line is from a model that includes Si II at the same velocity as He I, and although it produces a deeper absorption than observed, it shows a notch near 6200 Å that is similar in shape to the observed feature. The dotted line is from a model without Si II, and it fails to reproduce the observed inflection.

SYNOW can also produce a notch like the one found in the data when we include a high-velocity hydrogen line-forming region at 15,000 km s^{-1} in addition to the H layer that forms the primary absorption at 12,000 km s^{-1}. We model the HV region with a shallower optical depth profile ($n = 5$ instead of 6). The model with HV hydrogen only generates a detectable blue component for Hα. It does not generate similar HV notches for the other H I lines. That result is consistent with the observations that do not find HV components (notches at 15,000 km s^{-1}) for other H I lines (Figure 6).

In this case, SYNOW provides two plausible answers to the question about the source of the two-component line profile, but it does not give clear guidance to help us choose between them.

5.3. Ca II Features

The bottom left panel of Figure 11 shows that the Ca II H&K λ3945 feature (solid line) is successfully fit with a SYNOW model using an $n = 6$ optical depth profile (dashed line). However, the same model does not fit the observed Ca II infrared triplet (IR3, λ8579) seen in the bottom right of Figure 11. The IR3 forms a stronger and more extended absorption than the $n = 6$ model used to fit Ca II H&K. The model can be improved with respect to the IR3 feature by using a shallower optical depth profile ($n = 5$) or by inserting an HV Ca II layer, but both of

these solutions produce spectra that are incompatible with the observed Ca II H&K profile. The unusual IR3 profile may be caused by line blending and not HV Ca II, but we are unable to reproduce the observations of Ca II IR3 with any of the other ions expected to be found in Type II SN atmospheres (Hatano et al. 1999).

5.4. UV Flux Deficit

We also use SYNOW models to explore the steep drop in the continuum flux of SN 2011dh at the blue end of the *HST*/STIS spectrum compared to other SN IIb (Figure 5). This wavelength region is included in the lower left panel of Figure 11, but at this phase the data are from *Swift*/U-grism observations. The model spectrum plotted with a dashed line matches the data (solid line) reasonably well, and contributions from both Ti II and Co II are required to fit the observed UV-continuum level. The dotted line is produced by a model that omits both Ti II and Co II, and it clearly has excess flux at wavelengths less than 3700 Å. Despite the suggestion from SYNOW that Ti II and Co II are present, individual absorption features from Ti II and Co II are not identified in the *Swift* data from days 10 and 11 or the *HST* from day 24.

6. LIGHT CURVES

Figure 3 displays LCs for SN 2011dh in 12 filters covering 4–34 days after the explosion. For all figures and tables we express the times of observation in whole days relative to the estimated date of explosion. Data were obtained with *Swift* filters (*UVW2*, *UVM2*, *UVW1*, and *U*), FLWO/KeplerCam filters (u', B, V, r', and i'), and FLWO/PAIRITEL filters (J, H, and K_s). The measurements for each filter are listed by phase in Tables 3, 5, and 6. The data for bands from *UVW1* through i' were fit with a polynomial to estimate the peak luminosities and the times of maximum brightness that are displayed in Table 2.

All references to "peak" or "maximum" in the following discussion refer to the observations in this sample that cover the second, or radiation-powered, peak. We note that systematic offsets of 0.04–0.15 mag are found between the FLWO/KeplerCam $u'BVr'i'$ data and other published optical data (see Section 2.2). The data presented here are our measurements, and no offsets have been applied.

Evidence for cooling from the initial shock-heated peak can be seen in the first few observations that show a decline in brightness for the *U* band and bluer passbands. In our sample, minima are reached on day 5 for u', day 6 for *U* band, and day 7 for *UVW1*. The UV LCs subsequently rise toward a second peak as radioactivity in the core begins to provide the luminosity. At the phase of our first observations (4 days after the explosion) the LC for the *B* band is at minimum, and the LCs for all longer wavelength filters have passed their minima and are already rising toward the radiation peak. An initial decline was also observed at optical wavelengths in data of SN 2011dh obtained prior to day 4 (Maund et al. 2011; Arcavi et al. 2011; Bersten et al. 2012).

The *U*-band peak occurs on day 16, and as the filter wavelength increases, the time to peak increases. SN 2011dh reached a *B*-band peak of 13.18 mag on day 20.0 ± 0.5 and a *V*-band peak of 12.44 mag on day 20.6 ± 0.5. The dates and magnitudes of the JHK_s maxima are uncertain because we lack NIR photometry after day 24, although inspection of Figure 3 suggests that the NIR LCs are within a day or two of their maxima on day 24.

Figure 3 shows that LCs for all bands experience a relatively steep initial rise in brightness with a noticeable change in slope between days 9 and 12 to a more gradual rate of increase. This phase corresponds to the initial detection of He I. From that phase through the time of maximum brightness the rate of increase is slower. After the peak in each band, the decline is almost linear through the end of our data on day 34. This pattern is similar in all bands from *UVW1* to *H*, with the phase of the changes occurring earlier at shorter wavelengths. The LC of SN 2011dh presented by Sahu et al. (2013) and Ergon et al. (2013) also show this behavior.

The LC for *UVM2*, which is the shortest wavelength filter in our sample, declines steeply from the thermal peak through about day 15, but the subsequent radioactive diffusion is at too low a temperature to revive the LC. The luminosity in *UVW2* is essentially flat from day 6 through day 23, which is the time of bolometric maximum. *UVW1* is the bluest filter to exhibit a radiation-powered second peak.

The transmission curves of the *Swift*/UVOT *UVW1* and *UVW2* filters have extended red tails, so the measured flux in these bands includes a contribution from the red side that is beyond the intended wavelength region. We have shown that SN 2011dh has a very low UV flux during the time of our observations, and it is likely that there are significant contributions from optical wavelength regions to the *Swift* measurements in these filters. This "red leak" may contribute to the differences in timing of the minima and overall LC shape between the *UVM2* band and the *UVW1* and *UVW2* bands.

6.1. Photometric Colors

B- and *V*-band colors for SN 2011dh are plotted by phase in Figure 12. At day 4, the optical minus IR colors ($B - J$, $B - H$, $V - J$, $V - H$) are ≈0.5 mag redder than optical minus optical colors at this early phase. The optical minus IR colors rapidly become bluer at about 0.035 mag day^{-1} through day 9, while the optical minus optical colors show little change through day 11.

At about day 9, the optical minus IR colors reach a minimum and immediately start reddening, but with a slower rate of change. The timing of these minima coincides with transparency in the H shell since He I is first detected on day 11. This is also the phase when measured velocities of most absorption features stop their rapid decline (Figure 8). From day 10 through the time of maximum brightness (≈day 21) all colors shift gradually to the red, indicating that the atmosphere is cooling. After maximum, expansion continues to cool the SN, and the rate of reddening increases. The color evolution that we find for SN 2011dh agrees with the colors reported by Sahu et al. (2013) and Ergon et al. (2013).

The $B - V$ colors in SN 2011dh are similar to those of SN 1993J with a period of reddening through about day 8 followed by a very gradual reddening for about 2 weeks and then a steeper increase (Barbon et al. 1995; Richmond et al. 1996). $B - V$ in SN 2011dh is ≈0.2 mag greater from day 4 to day 22 but very close to $B - V$ in SN 1993J from day 22 through the end of our observations.

From day 4 to day 20, $B - V$ development in SN 2008ax is very similar to the $B - i'$ behavior observed in SN 2011dh. The color gets bluer from the initial measurement, reaches a minimum near 0.2 mag on day 12, and then begins to redden. By day 22, $B - V$ in SN 2008ax is close to the same values found in SN 201dh and SN 1993J. For both SN 1993J and 2008ax, $B - V$ stops increasing on about day 40.

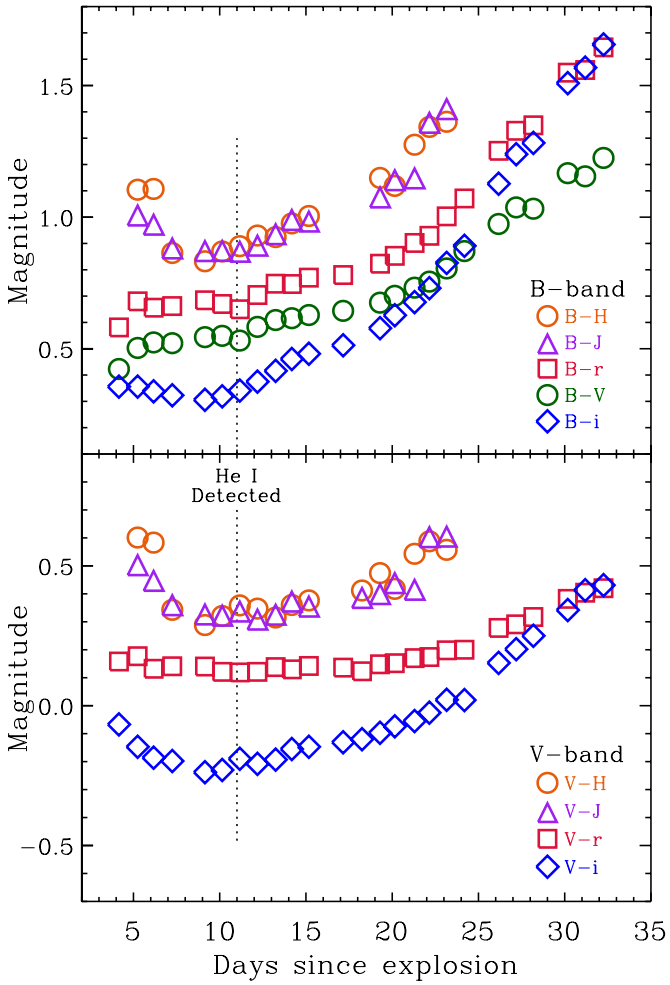

Figure 12. *B*- and *V*-band colors for SN 2011dh. The optical minus NIR colors are redder at the earliest observations and decline rapidly through day 9, while optical minus optical colors are bluer in the initial observations and remain nearly constant over days 4–9. All colors redden from day 10 through day 34, which indicates the atmosphere is cooling.

(A color version of this figure is available in the online journal.)

Table 9
Bolometric Luminosity by Phase

Epoch[a] (days)	Total Flux [b] (10^{42} erg s^{-1})	NIR Flux (10^{42} erg s^{-1})	NIR Fraction	UV Flux (10^{42} erg s^{-1})	UV Fraction
4	0.29	0.09	0.31	0.05	0.16
5	0.35	0.11	0.31	0.04	0.11
6	0.43	0.14	0.32	0.03	0.08
7	0.56	0.17	0.31	0.04	0.06
8	0.67	0.21	0.31	0.04	0.06
9	0.80	0.24	0.31	0.04	0.05
10	0.94	0.30	0.32	0.05	0.05
11	1.05	0.33	0.32	0.05	0.05
12	1.17	0.37	0.32	0.05	0.04
13	1.27	0.41	0.32	0.05	0.04
14	1.34	0.44	0.33	0.05	0.04
15	1.43	0.47	0.33	0.05	0.04
16	1.52	0.51	0.34	0.06	0.04
17	1.59	0.54	0.34	0.06	0.04
18	1.65	0.56	0.34	0.06	0.04
19	1.69	0.58	0.34	0.06	0.03
20	1.74	0.61	0.35	0.06	0.03
21	1.77	0.62	0.35	0.05	0.03
22	1.78	0.64	0.36	0.05	0.03
23	1.78	0.68	0.38	0.04	0.03
24	1.73	0.67	0.39	0.04	0.02
25	1.65	0.67	0.40	0.03	0.02
26	1.58	0.66	0.42	0.03	0.02
27	1.48	0.63	0.43	0.03	0.02
28	1.39	0.61	0.44	0.02	0.02
29	1.29	0.58	0.45	0.02	0.01
30	1.21	0.55	0.46	0.02	0.01
31	1.14	0.54	0.47	0.01	0.01
32	1.07	0.51	0.47	0.01	0.01
33	1.01	0.49	0.48	0.01	0.01
34	0.97	0.47	0.49	0.01	0.01

Notes.
[a] Whole days with respect to the time of explosion.
[b] Total measurement uncertainties are ≈10% of the bolometric flux.

The $V-R$ color curve of SN 2011dh is generally similar to $V-R$ color behavior in SN Ib and SN Ic found by Drout et al. (2011). These SN types are similar to SN IIb in that they are core-collapse events with little or no hydrogen in the spectra. The mean $V-R$ values from Drout et al. (2011) display an early decline through day 12 (with respect to the explosion), a period of little change through day 20, and an increase through about day 36. The $V-R$ curve in SN 2011dh is slightly flatter, but $V-i'$ is a close match.

7. BOLOMETRIC LIGHT CURVE

We construct a bolometric LC for SN 2011dh from UVOIR data obtained by *Swift*, KeplerCam, and PAIRITEL. The flux measurements are given by phase in Table 9, and the LC is plotted in Figure 13. A second bolometric LC for SN 2011dh, compiled by Ergon et al. (2013) from a different data set, is also displayed. Bolometric LCs for two other Type IIb SN are also displayed. SN 1993J (Richmond et al. 1994) is shown with green triangles, and 2008ax (Pastorello et al. 2008) is plotted with purple diamonds.

The spectral energy distributions (SEDs) were sampled at the central wavelength of each observed passband. Measurements were corrected for Galactic reddening $E(B-V) = 0.035$ mag using the total-to-selective extinction ratios for all filters given in Schlegel et al. (1998). Magnitudes were converted to quasi-monochromatic flux densities using the central wavelengths for each filter as listed in Table 2. The flux was integrated by wavelength using a simple trapezoidal rule. The UV contribution was determined by integrating the reddening-corrected *Swift UV fluxes* for filters *UVW2, UVM2*, and *UVW1*. The missing far-UV fluxes were estimated by assuming zero flux at 1000 Å and approximating the SED with a straight line between 1000 Å and $\lambda_c(UVW2) = 2030$ Å. The missing mid-IR flux was approximated by integrating the Rayleigh–Jeans tail of a blackbody from the flux measured at the central wavelength of the reddest filter to infinity. The total measurement uncertainties are ≈10%.

The maximum bolometric luminosity of 1.8×10^{42} erg s^{-1} was reached about 22 days after the explosion (Table 9). NIR contributions to the total bolometric flux account for about 30% of the total bolometric flux from day 4 through the bolometric maximum. After maximum, the NIR fraction increases, and it reaches 49% on day 34. The UV fraction of the total is 16% on day 4, and it declines rapidly to 5% on day 9 and then to 1% on day 29.

Our results for the bolometric luminosity and fractional contributions of the UV and NIR agree with the results presented by Ergon et al. (2013) and by Lyman et al. (2013). Figure 13

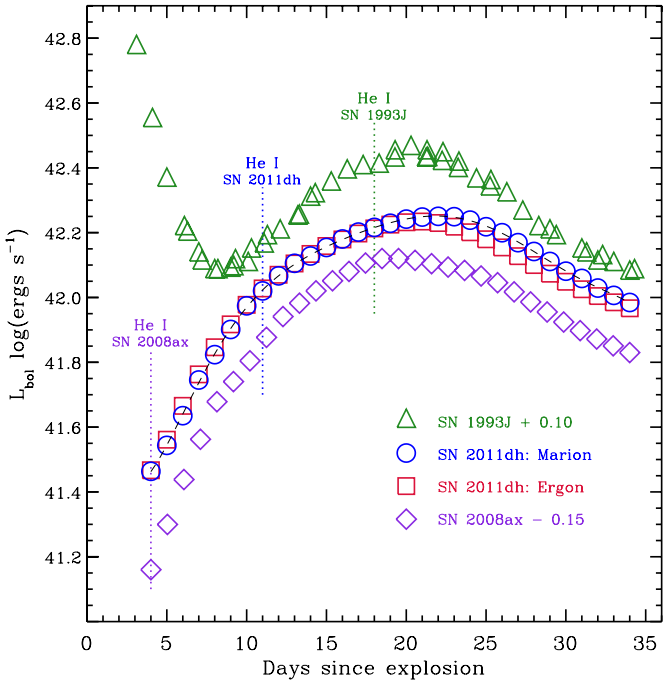

Figure 13. Bolometric light curves of three SN IIb. SN 1993J (Richmond et al. 1994) is displayed as green triangles and is shifted up by 0.10 log(erg s^{-1}) for clarity. SN 2011dh data from this paper are displayed with blue circles, and SN 2011dh data from Ergon et al. (2013) are shown as red squares. SN 2008ax (Pastorello et al. 2009) is plotted with purple diamonds, and the LC is shifted down by 0.15 log(erg s^{-1}). The LC for the three SN IIb LCs are very different for the first 12 days, but the maximum luminosities, times of maxima, and decline rates are similar. The phases at which He I was first detected in each of the SN IIb are marked with the same colors as the symbols.

(A color version of this figure is available in the online journal.)

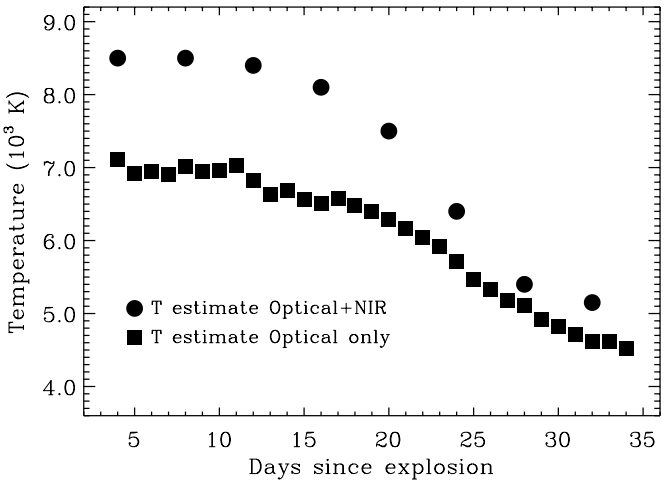

Figure 14. Estimated temperature by phase for SN 2011dh from 4 to 34 days after the explosion. The circles are temperature estimates based on blackbody fits that include NIR data. The squares are temperature estimates made using optical data only.

shows that the bolometric LC for SN 2011dh from this paper and that from Ergon et al. (2013) are very close before the bolometric maximum. After maximum there is a small divergence due to the way that the NIR contribution is calculated. Our sample lacks NIR photometry after day 22. From 23 to 34 days the reddest filter in our sample is i'. That means that the blackbody used to estimate the missing IR flux begins at 0.775 μm. Ergon et al. (2013) include MIR data from *Spitzer*, and they calculate the missing IR contribution with a blackbody beginning at 4.5 μm.

The Richmond et al. (1994) bolometric LC for SN 1993J in Figure 13 is based on optical (*UBVRI*) observations. The missing contributions on both the blue and red sides are estimated by using the optical data to establish a temperature at each phase. The amount of blackbody flux that would be emitted outside the *UBVRI* window is added to the total from the optical measurements. The bolometric LC for SN 2008ax was produced by Pastorello et al. (2008). They compiled several data sets of SN 1993J to construct a new UVOIR LC and then rescaled the *UBVRI* data for SN 2008ax data using the same fractional NIR contribution estimated for SN 1993J.

The early LC from SN IIb 2011dh, 2008ax, and 1993J have very different shapes due to differences in the cooling times of the shock-heated material surrounding each SN. However, the maximum bolometric luminosities, the times of maxima, the decline rates, and the $B-V$ colors are similar for all three SN IIb. The near uniformity in the bolometric LCs after the first few days suggests that the hydrogen shells only affect the LCs during the early, cooling phase. The similar bolometric luminosities suggest that the ^{56}Ni yields must have been close to the same for each explosion. These conclusions are all consistent with progenitors of SN IIb having similar compositions and masses, but they explode inside hydrogen envelopes that can vary significantly.

8. TEMPERATURES

Figure 14 shows estimated temperatures for SN 2011dh by phase. The filled circles are temperature estimates obtained by fitting BB curves by eye to a full set of optical and NIR SEDs from passbands $BVr'i'JHK$. The filled squares are temperature estimates using only optical SEDs ($BVr'i'$) that are fit to BB curves by minimizing χ^2. Both methods suggest very little change in temperature from day 4 to day 12, which is consistent with nearly constant values for $B-V$ during this epoch. The phase at which the temperature begins to decline is also when the H layer becomes transparent and reveals the He region below.

Figure 2 shows BB curves fit to the optical and NIR spectra obtained 8, 12, and 16 days after the explosion. We find a very consistent relationship between BB temperature curves, the complete optical and NIR spectra, and the SEDs for optical and NIR passbands $u'BVr'i'JHK$. We do not plot SEDs on the already crowded Figure 2, but the temperature curves fit to optical and NIR spectra pass directly through the SEDs for passbands $Vi'JHK$ at all three phases. The circles in Figure 14 represent the temperature of a BB curve that we chose by eye to fit the $Vi'JHK$ SEDs. Line blending is less severe in the NIR than at UV and optical wavelengths, which puts an additional premium on the PAIRITEL data that are available through day 24. After day 24, we replace the JHK SEDs by integrating the Rayleigh–Jeans tail of a blackbody.

The SEDs for u', B, and r' are less reliable. For example, the r'-band SED is complicated by the large Hα absorption feature in spectra of SN 2011dh. BB curves that pass through the V-band and i'-band SEDs are always a little below the r'-band SED. The suppressed continuum flux for SN 2011dh at less than 4000 Å means that a blackbody is not a realistic representation of data from SN 2011dh at these wavelengths. That means that any method of estimating temperature with BB curves does not actually fit data to the peak of the BB curves.

Temperature estimates made by fitting to a wider wavelength range that includes the NIR appear to be more effective than

estimates made with optical data alone. Our estimate for the day 4 temperature is 8500 K, which is ≈1000 K higher than the temperature estimate for a day 3 optical spectrum provided by Arcavi et al. (2011) and ≈700 K higher than the estimate of Bersten et al. (2012).

9. SUMMARY AND CONCLUSIONS

Our results show details of chemical layering in SN 2011dh that have not been previously reported for SN IIb. We demonstrate the importance of NIR measurements for line identification, temperature estimates, and bolometric estimates.

A UV spectrum from *HST*/STIS shows a significant deficit in continuum flux at wavelengths below 4000 Å when compared with other SN IIb. SYNOW model spectra are used to demonstrate that line blanketing from Ti II and Co II are responsible for the suppressed UV flux. We also use SYNOW models to investigate blended features and to support spectral evidence for the presence of He I in a spectrum obtained on day 11.

Velocities of H I, He I, Ca II, and Fe II lines are measured from 4 days after the explosion through day 34. All velocities are at maximum in the earliest observations and decline rapidly to about day 10. The change in the decline rate coincides with the first detection of He I in the spectra. H I and He I velocities become constant by day 20, while Ca II and Fe II velocities continue to decline. The relative velocities between ions and the velocity decline rates found in SN 2011dh are similar to observations of SN IIb 1993J and SN IIb 2008ax.

We show that early measurements of both H I and He I are important for understanding the transition in SN IIb from the early phases when hydrogen dominates the spectra to later times when H fades and He becomes dominant. We present the earliest secure identification of He I lines in spectra of SN 2011dh. NIR spectra confirm that He I is present 11 days after the explosion. Using measurements of four H I lines and five He I lines, we show that the H and He line-forming regions are separated by ≈4000 km s^{-1} at all phases. We suggest that this gap is consistent with an optically thick, H-rich shell that encloses the explosion and conceals material beneath it. In SN 2011dh, expansion makes the H shell transparent and reveals the slower-moving He-rich region on about day 11.

Using the time intervals from the explosion to the first detection of He I, we estimate the relative masses for the hydrogen-rich envelopes surrounding three SN IIb. We estimate that the mass of the hydrogen shell surrounding the progenitor of SN 2011dh was about three times more massive than the shell around SN 2008ax but about eight times less massive than the shell that enclosed SN 1993J.

We present photometry of SN 2011dh from 12 filters and construct a bolometric LC that has a maximum luminosity of $1.8 \pm 0.2 \times 10^{42}$ erg s^{-1} on day 22. The NIR fraction of the total bolometric luminosity in SN 2011dh is 31% on day 4, and it rises to 49% on day 34. The UV contribution to the total flux is 16% on day 4, declining to 5% on day 9 and to 1% on day 29.

We compare the bolometric LCs for SN IIb 2011dh, SN IIb 2008ax, and SN IIb 1993J. The LC display significant differences in the first 12 days after the explosion due to different cooling times of the shocked regions. At subsequent phases, however, the LC for the three SN IIb are very similar. Thus, the hydrogen shell mass appears to influence only the very early LCs of these SN IIb. The agreement of the bolometric luminosities, the times of the maxima, the decline rates, and the $B - V$ colors for these three SN IIb suggests that the progenitors may have had similar masses and composition when they exploded inside hydrogen shells of differing masses and distributions.

The progenitor of SN 2011dh has recently been identified as a yellow supergiant star. Successful models based on that progenitor will have to match the detailed velocity measurements and LC data presented here.

The CfA Supernova Program is supported by NSF grant AST-1211196 to the Harvard College Observatory. R.P.K. was supported in part by the National Science Foundation under grant NSF PHY-1125915 to the Kavli Institute for Theoretical Physics. J.V. is supported by Hungarian OTKA grants K-76816 and NN-107637, NSF grant AST-0707769, and Texas Advanced Research Project ARP-009. J.C.W. is supported by NSF grant AST-1109801. A.S.F. acknowledges support from a NSF Graduate Research Fellowship and a NASA Graduate Research Program Fellowship. Support for program GO-12540 was provided by NASA through a grant from the Space Telescope Science Institute, which is operated by the Association of Universities for Research in Astronomy, Inc., under NASA contract NAS5-26555. K.T. has also received support from Hungarian OTKA grant K-76816.

G.H.M. thanks John Rayner, Alan Tokunaga, Bill Golish, David Griep, Paul Sears, and Eric Volquardsen at the IRTF for supporting target-of-opportunity observations. G.H.M. is a visiting astronomer at the Infrared Telescope Facility, which is operated by the University of Hawaii under Cooperative Agreement NNX-08AE38A with the National Aeronautics and Space Administration, Science Mission Directorate, Planetary Astronomy Program. We thank Gaspar Bakos, David Latham, and Matthew Holman for making FLWO observing time available. We acknowledge the work of C. Klein on the PAIRITEL mosaic data reduction pipeline, and we reference observations made with the Vatican Advanced Technology Telescope. The authors make frequent use of David Bishop's excellent Web page listing recent supernovae and valuable references associated with them: http://www.rochesterastronomy.org/snimages/.

Facilities: HST (STIS), FLWO:1.5m (FAST), HET (LRS), *Swift* (UVOT; UV grism), IRTF (SpeX), FLWO:1.2m (KepCam)

REFERENCES

Arcavi, I., Abdou, Y., Abu-Zayyad, T., et al. 2011, ApJ, 742, 18
Arnett, W. D., Bahcall, J. N., Kirshner, R. P., & Woosley, S. E. 1989, ARA&A, 27, 629
Barbon, R., Benetti, S., Cappellaro, E., et al. 1995, A&AS, 110, 513
Benvenuto, O. G., Bersten, M. C., & Nomoto, K. 2013, ApJ, 762, 74
Bersten, M. C., Benvenuto, O. G., Nomoto, K., et al. 2012, ApJ, 757, 31
Bietenholz, M. F., Brunthaler, A., Soderberg, A. M., et al. 2012, ApJ, 751, 125
Branch, D., Baron, E. A., & Jeffery, D. J. 2003, in Lecture Notes in Physics, Vol. 598, Supernovae and Gamma-Ray Bursters, ed. K. Weiler (New York: Springer), 47
Branch, D., Benetti, S., Kasen, D., et al. 2002, ApJ, 566, 1005
Chevalier, R. A., & Soderberg, A. M. 2010, ApJ, 711, 40
Chiosi, C., & Maeder, A. 1986, ARA&A, 24, 329
Chonis, T. S., & Gaskell, C. M. 2008, AJ, 135, 264
Chornock, R., Filippenko, A. V., Li, W., et al. 2011, ApJ, 739, 41
Chugai, N. N., Chevalier, R. A., & Utrobin, V. P. 2007, ApJ, 662, 1136
Cohen, M., Wheaton, W. A., & Megeath, S. T. 2003, AJ, 126, 1090
Cushing, M. C., Vacca, W. D., & Rayner, J. T. 2004, PASP, 116, 362
Dessart, L., Hillier, D. J., Livne, E., et al. 2011, MNRAS, 414, 2985
Drout, M., Soderberg, A. M., Gal-Yam, A., et al. 2011, ApJ, 741, 97
Ergon, M., Sollerman, J., Fraser, M., et al. 2013, A&A, in press (arXiv:1305.1851)
Fabricant, D., Cheimets, P., Caldwell, N., & Geary, J. 1998, PASP, 110, 79
Feldmeier, J. J., Ciardullo, R., & Jacoby, G. H. 1997, ApJ, 479, 231
Filippenko, A. V., Matheson, T., & Ho, L. C. 1993, ApJ, 415, 103

Friedman, A. S. 2012, Harvard University, PhD thesis
Hatano, K., Branch, D., Fisher, A., Millard, J., & Baron, E. 1999, ApJS, 121, 233
Hicken, M., Challis, P., Kirshner, R. P., et al. 2012, ApJS, 200, 12
Hicken, M., Garnavich, P. M., Prieto, J. L., et al. 2007, ApJL, 669, L17
Hill, G. J., Nicklas, H. E., MacQueen, P. J., et al. 1998, Proc. SPIE, 3355, 375
Horesh, A., Stockdale, C., Fox, D. B., et al. 2013, MNRAS, 436, 1258
Jeffery, D. J., Kirshner, R. P., Challis, P. M., et al. 1994, ApJL, 421, 27
Krauss, M. I., Soderberg, A. M., Chomiuk, L., et al. 2012, ApJL, 750, 40
Kumar, B., Pandey, S. B., & Sahu, D. K. 2013, MNRAS, 431, 308
Landolt, A. U. 1992, AJ, 104, 340
Lewis, J. R., Walton, N. A., Meikle, W. P. S., et al. 1994, MNRAS, 266, 27
Lyman, J., Bersier, D., & James, P. 2013, MNRAS, in press
Marion, G. H., Kirshner, R., Wheeler, J. C., et al. 2011, ATel, 3435
Matheson, T., Blondin, S., Foley, R. J., et al. 2005, AJ, 129, 2352
Maund, J. R., Fraser, M., Ergon, M., et al. 2011, ApJL, 739, 37
Mazzali, P. A., Benetti, S., Altavilla, G., et al. 2005, ApJL, 623, L37
Milisavljevic, D., Margutti, R., Soderberg, A. M., et al. 2013, ApJ, 767, 71
Modjaz, M., Li, W., Butler, N., et al. 2009, ApJ, 702, 226
Murphy, J. W., Jennings, Z. G., Williams, B., Dalcanton, J. J., & Dolphin, A. E. 2011, ApJ, 742, 4
Nomoto, K., Suzuki, T., Shigeyama, T., et al. 1993, Natur, 364, 507
Nomoto, K. I., Iwamoto, K., & Suzuki, T. 1995, PhR, 256, 173
Pastorello, A., Quimby, R. M., Smartt, S. J., et al. 2008, MNRAS, 389, 131
Pastorello, A., Valenti, S., Zampieri, L., et al. 2009, MNRAS, 394, 2266
Podsiadlowski, P., Hsu, J. J. L., Joss, P. C., & Ross, R. R. 1993, Natur, 364, 509
Prieto, J. L., & Hornoch, K. 2011, ATel, 3433
Ramsey, L. W., Adams, M. T., Barnes, T. G., et al. 1998, Proc. SPIE, 3352, 34
Rayner, J. T., Toomey, D. W., Onaka, P. M., et al. 2003, PASP, 115, 362
Reiland, T., Griga, T., Riou, A., & Lamotte Bailey, S. 2011, CBET, 2736
Richmond, M. W., Treffers, R. R., Filippenko, A. V., & Paik, Y. 1996, AJ, 112, 732
Richmond, M. W., Treffers, R. R., Filippenko, A. V., et al. 1994, AJ, 107, 1022
Ritchey, A. M., & Wallerstein, G. 2012, ApJ, 748, 11
Roming, P. W. 2009, ApJ, 704, 118
Rush, B., Malkan, M. A., & Edelson, R. A. 1996, ApJ, 473, 130
Sahu, D. K., Anupama, G. C., & Chakradhari, N. K. 2013, MNRAS, 433, 2
Schlegel, D. J., Finkbeiner, D. P., & Davis, M. 1998, ApJ, 500, 525
Schmidt, B., Kirshner, R. P., Eastman, R. G., et al. 1993, Natur, 364, 600
Silverman, J. M., Filippenko, A. V., & Cenko, S. B. 2011, ATel, 3398
Smith, J. A., Tucker, D. L., Kent, S., et al. 2002, AJ, 123, 2121
Soderberg, A., Margutti, R., Zauderer, B. A., et al. 2012, ApJ, 752, 78
Taubenberger, S., Navasardyan, H., Maurer, J. I., et al. 2011, MNRAS, 413, 2140
Tonry, J. L., Dressler, A., Blakeslee, J. P., et al. 2001, ApJ, 546, 681
Tsvetkov, D. Yu., Volkov, I. M., Sorokina, E. I., et al. 2012, PZ, 32, 6
Tully, R. B. 1988, VizieR On-line Data Catalog: VII/145, Nearby Galaxies Catalogue (Cambridge: Cambridge Univ. Press)
Van Dyk, S. D., Li, W., Cenko, S. B., et al. 2011, ApJ, 741, 28
Van Dyk, S. D., Zheng, W., Clubb, K. I., et al. 2013, ApJL, 772, L32
Vinkó, J., Takáts, K., Szalai, T., et al. 2012, A&A, 540, 93
Wheeler, J. C., Barker, E., Benjamin, R., et al. 1993, ApJ, 417, 71
Woosley, S. E., Eastman, R. G., Weaver, T. A., & Pinto, P. A. 1994, ApJ, 429, 300